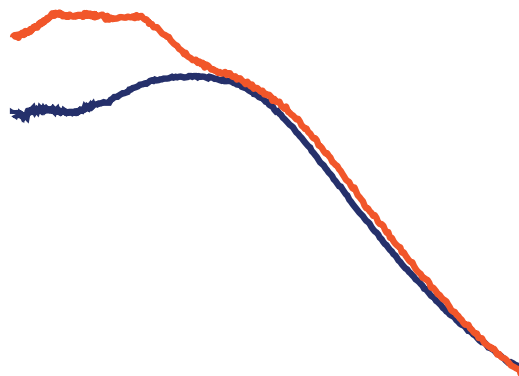


Towards controlling the Fermi energy in topological materials

MSc. Thesis Applied Physics
Quantum Transport in Matter
Interfaces and Correlated Electron Systems
Faculty TNW
University of Twente



February 14, 2014

Author:
Sam Slöetjes

Committee:
Prof. Dr. Ir. Alexander Brinkman
Marieke Snelder, MSc.
Assoc. Prof. Dr. Geert Brocks

Abstract

P-wave superconductivity can arise in topological insulator/s-wave superconductor hybrid systems. In this thesis it is theoretically investigated if this can also happen if the topological insulator is replaced by a metal with spin-orbit coupling. The analysis is done assuming a fully transparent barrier between the two materials, using techniques from BCS theory. It is found that the presence of the spin-orbit coupling term in the Hamiltonian gives an order parameter that has a full p-wave pairing symmetry.

Experimentally, transport measurements have been done on 50 and 100 *nm* thick flakes of the topological insulator material $\text{Bi}_{1.5}\text{Sb}_{0.5}\text{Te}_{1.7}\text{Se}_{1.3}$. A back gate voltage was applied to observe if the Fermi energy can be controlled. From $\rho_{xx}(T)$ measurements it is found that the surface contribution to conductivity is influenced by the back-gate. Measurements of ρ_{xx} as a function of applied gate voltage show an increasing resistance with a decreasing gate voltage, but no sign of the Dirac point. The Hall resistivity was measured for gate voltages of -21, 0 and 21 *V* and the approximate carrier density and mobility were found. The carriers are found to be n-type and the carrier density increases with increasing gate voltage. The mobility decreased for both positive and negative gate voltages, indicating that the gate voltage dependence in the resistivity measurements is not only the result of a modulated Fermi energy.

Contents

1	Introduction	7
1.1	Goal and outline of this thesis	7
1.2	Introduction to superconductors	7
1.3	What is a topological insulator?	8
1.3.1	Connection to Topology	9
1.4	A short history of BSTS	10
1.5	A way to control the Fermi level	13
1.6	Current state in the search for the Majorana fermion	14
2	Modelling a p-wave superconductor	17
2.1	Characterizing the excitations of an s-wave superconductor via the BCS Hamiltonian	17
2.2	Majorana fermions in a p-wave superconductor	19
2.3	A conventional s-wave superconductor in proximity to a topological insulator	21
2.4	The s-wave superconductor in proximity to a metal with spin-orbit coupling	23
2.4.1	Model Hamiltonian for a metal with spin-orbit coupling	23
2.4.2	A metal with spin-orbit coupling and the s-wave superconductor	25
2.5	Majorana fermions?	26
2.6	Recommendations	26
2.7	The importance of gating	26
3	Set-up and sample preparation	29
3.1	Applying BSTS to the substrate	29
3.2	Preparing the contacts by photolithography	29
3.3	Preparing the contacts by electron beam lithography	30
3.4	Back-gate contact and the connection to the measurement apparatus	31
3.5	Measurement set-up	32
4	Transport measurements on BSTS with an applied gate voltage	35
4.1	ρ_{xx} as a function of the temperature	35
4.2	ρ_{xx} as a function of the gate voltage	37
4.3	Carrier density and mobility as a function of gate voltage	38
4.4	Conclusion and outlook	39
A	Parameters for electron beam deposition	41
	Acknowledgements	44
	Bibliography	47

Chapter 1

Introduction

In 1937 Ettore Majorana found a solution to the Dirac equation that would imply that fermionic particles could exist that are their own anti-particles [1, 2], now called Majorana fermions. From then on a hunt for particles that are potential Majorana fermions started, mainly in the field of high energy physics [3]. In 2008, it was predicted by Fu and Kane that states could exist in condensed matter systems that obey these Majorana-statistics, using combinations of low temperature superconductors and a new type of material, the ‘topological insulator’ [4]. In condensed matter physics, these Majorana states are interesting because of their special exchange statistics. For example, when one interchanges two Majorana bound states (MBS) spatially, the total wavefunction of the system does not simply obtain a minus sign as in the case of normal fermions. Also, these particles are topologically protected against decoherence. These properties make that the Majorana fermion is the most promising candidate for qubits, the main ingredient for the realisation of a quantum computer, which is expected to execute calculations much faster than a digital computer.

1.1 Goal and outline of this thesis

The goal in this thesis is to find the right circumstances for the Majorana fermions. This will be done by theoretically investigating how simple a system that can host a MBS can be made, and experimentally by finding a way to tweak the Fermi level in BSTS. BSTS is a very new topological insulator, a necessary ingredient as mentioned above.

In the following sections an introduction to the concept of the superconductor and the Majorana fermion, the topological insulator, the material BSTS and the electric field effect (gating) will be given. Also the current state in the search for Majorana fermions will be quickly reviewed. In chapter two, we dive a little bit deeper and show (in the language of second quantization) how the Majorana bound state emerges in a p-wave superconductor (a special type of superconductor). After this we will see how it emerges in a hybrid system. The set-up and sample preparation for the gating measurements are discussed in chapter 3, introducing the experimental aspects, and finally in chapter 4 the results of subsequent measurements are showed and discussed.

1.2 Introduction to superconductors

Superconductors are materials that can conduct electricity with zero resistance at very low temperatures, first experimentally found in 1911 [5]. In this section, we will explain

the basic mechanism behind superconductivity and why the superconductor is a natural hunting ground for Majorana fermions.

In a normal (s-wave) superconductor, the electrons in the material pair up to become Cooper pairs, these two electrons have opposite spin and momentum (k, \uparrow) and $(-k, \downarrow)$. Cooper showed that this attractive interaction lowers the energy of the electron gas [6]. The two electrons pair up due to an attractive interaction that is mediated by phonons.

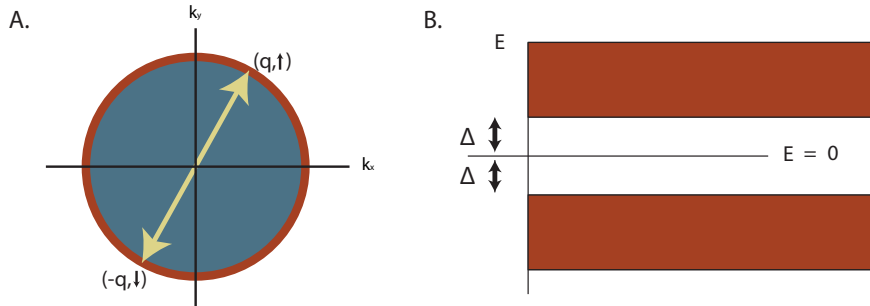


Figure 1.1: A. The pairing two electrons in the vicinity of the Fermi energy. B. Filled states separated with a gap Δ from the Fermi energy ($E = 0$)

The Cooper pairs are bosons (because they are compositions of two fermions) which (below the critical temperature) condense in the lowest energy state of the system, analogous to Bose-Einstein condensation. At zero temperature, all the electrons in the system have formed Cooper pairs. In BCS theory, at finite temperature, the electrons that do not contribute to the condensate are broken Cooper pairs and are called ‘quasiparticles’. In terms of energy, at a finite temperature the condensate resides at the Fermi energy, and the quasiparticle excitations are separated from the Fermi energy by a gap of magnitude Δ , as illustrated in 1.1B. Because of this gap, there are no states in the vicinity of the state where the condensate resides to scatter to, this means that scattering is suppressed for pairs in the condensate and hence the resistance goes to zero. The excitations in a superconductor have the form of a superposition of an electron and a hole. Knowing that the antiparticle of an electron is a hole and the antiparticle of a hole is an electron, these excitations are a potential source for fermionic particles that are their own antiparticles (i.e. Majorana fermions) [7, 8]. As will be shown in chapter 2, s-wave superconductors cannot host Majorana fermion, for that we have to turn to a different type of superconductor: the p-wave superconductor. A p-wave superconductor can be engineered by combining an s-wave superconductor and a novel material: a topological insulator.

1.3 What is a topological insulator?

A topological insulator (TI) is a material that is insulating in the bulk and conducting on the surface. In this section we will roughly explain how a TI works and what it has to do with topology, starting with the introduction of the quantum Hall effect.

The quantum Hall effect (QHE) is the effect of quantized conductance due to edge modes in an effectively 2D material when a strong magnetic field is switched on [9]. In the quantum *spin* Hall effect the spin degeneracy is eliminated, by spin-splitting of the edge modes [10, 11, 12]. The spin-direction is in this case locked to the direction of motion of the electron, see figure 1.2. In the quantum spin Hall effect, the electrons in the edge states are prohibited from backscattering by destructive interference of their wavefunction

due to the extra phase they pick up as a result of presence of the magnetic field. This geometric phase is called the ‘Berry’s phase’ [13].

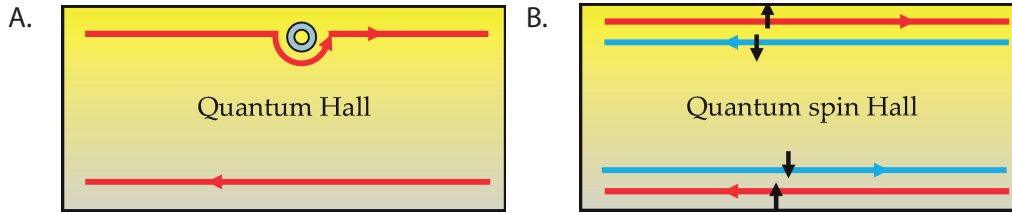


Figure 1.2: A. The quantum Hall effect: when a material is placed in a strong perpendicular magnetic field, edge states arise, quantizing the conductivity. B. Under some circumstances, these edge states can be spin split, resulting in a spin polarized conductance: spin up only goes one way, spin down only goes the opposite way. Figure from [14].

In 2006 it was predicted [15] that HgTe/CdTe wells could feature the quantum spin Hall effect in the absence of a magnetic field, when reaching a certain critical thickness. At this critical thickness, the electronic state is ‘inverted’, which corresponds to a topological phase transition in the band structure of the well. Later experiments confirmed this effect [16].

1.3.1 Connection to Topology

Topology is the branch in mathematics concerned with the properties of space that are preserved under continuous deformations including stretching or bending, but not gluing or tearing. Consider an orange, which can be continuously deformed into a pillow or a couch but not into a donut, because in order to make a donut, one has to tear a hole in the orange. We associate this with a topological number, the genus (g), which corresponds to the number of holes in an object. In that case, an orange has $g = 0$ and a donut has $g = 1$, in order to make an orange into a donut, we say that it has to go through a topological phase transition.

In band theory, one can assign a topological number to the way the bands are arranged in a band structure. In the case of the HgTe/CdTe well, the bands in the HgTe well are inverted with respect to the CdTe around it, i.e. the well has a different topological number than the CdTe. At the interface (the edge), the band structures have to be connected, hence a crossing of the bands takes place, bridging the bandgap of the materials, and in this way establishing conducting surface states.

In 2007, it was predicted that this same effect could occur in three dimensions. $\text{Bi}_{1-x}\text{Se}_x$, a material with an inversion symmetry in the lattice, was proposed to have conducting ‘surface states’ (the 2D analogue of the 1D edge state) [17, 18], and was later confirmed to have these characteristics in the bandstructure [19, 20]. This property of spin-split surface states is partly the result of a large ‘spin-orbit coupling’, a term that will be further explained in the second chapter. This spin-orbit coupling effect results in the spin split bands that connect the valence and the conduction band in the bandstructure, see figure 1.3. Later on, Bi_2Se_3 , Bi_2Sb_3 and Bi_2Te_3 were also predicted to have these surface states, based on first principle electronic structure calculations [21]. It must be said that, although they are called topological insulators, the bandgap of current topological insulators is in the order of $\sim 0.1 \text{ eV}$, which is typically a semiconductor bandgap.

In this project, experiments will be done on a new topological insulator called ‘BSTS’, mainly to inspect if the Fermi level can be controlled.

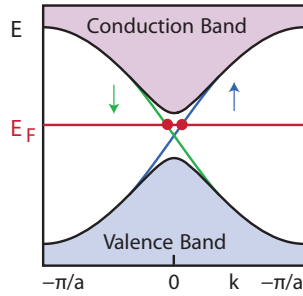


Figure 1.3: The spin orbit coupled bands that connect the valence and the conduction bands that are gapped. When zoomed in, these spin orbit coupled bands (in 3D) trace out a cone, called the ‘Dirac cone’, similar to the cone in graphene. Figure from [22].

1.4 A short history of BSTS

When the TIs Bi_2Se_3 , Bi_2Sb_3 and Bi_2Te_3 were discovered, immediately experiments began to optimise the topological nature of these materials.

Taskin et al. [23] tried to do this by combining separate elements, for instance with $\text{Bi}_2\text{Te}_2\text{Se}$ (BTS). In figure 1.4, angle-resolved photoelectron spectroscopy (ARPES) measurements of BTS are shown, made by Arakane et al. [24]. The bandstructure of the gapped region is made visible with this technique. It can be seen in figure 1.4B that the Fermi level lies in the electron doped region. From this picture it can also be seen that the crossing of the surface states, the ‘Dirac point’, lies very close to the valence band. Figure 1.4A, shows the cross-section of the Dirac cone for various energies, showing that the Fermi surface is not perfectly round, but slightly hexagonal, due to an effect called ‘warping’, which can be explained in the framework of $\mathbf{k} \cdot \mathbf{p}$ -theory [25].

It was found for BTS that the surface channel contributes up to 6 percent of the total conductance (for a crystal of 30 μm thickness), which implies a large bulk contribution. When Sb was introduced into some of the Bi positions of the BTS, a new TI was born: $\text{Bi}_{2-x}\text{Sb}_x\text{Te}_{3-y}\text{Se}_y$. For $\text{Bi}_{1.5}\text{Sb}_{0.5}\text{Te}_{1.7}\text{Se}_{1.3}$ (the TI used in this project, from now on called ‘BSTS’) it was measured that the surface channel could contribute up to 70 percent of the total conductance [23]. ARPES measurements were done by [24], for four different values of (x,y), namely (0,1) (BTS), (0.25,1.1), (0.5,1.3) (BSTS) and (1,2), as shown in figure 1.5A and B. Figure 1.5A shows the Fermi surface for the different compositions, and can be seen to decrease in radius, with an increasing amount of Sb and Se. Figure 1.5B shows the shift in the position of the Dirac cone. It can be seen that for BTS, the Dirac point (E_{DP}) lies below the boundary of the valence band (E_{VB}). When the concentrations of Sb and Se are increased, the position of the Dirac point becomes higher, rising above the boundary of the valence band. This is illustrated schematically in figure 1.5C, from which it can be seen that the BSTS features n-type Dirac-like transport.

The crystals that were grown for the group that made the ARPES measurements are made by a different group than the ones used in this project. The crystals in this project were manufactured by the group ‘Quantum electron matter’ from the University of Amsterdam, in this case (ARPES) measurements were also done, as shown in figure 1.6B and C. From these measurements, it is visible that the BSTS used in this project also has a Dirac point that lies above the valence band, and a Fermi level in the electron-like part of the Dirac cone. The basic structure unit of the BSTS is shown in figure 1.6A. One can observe that the unit cell is built from five layers stacked on top of each other, this is

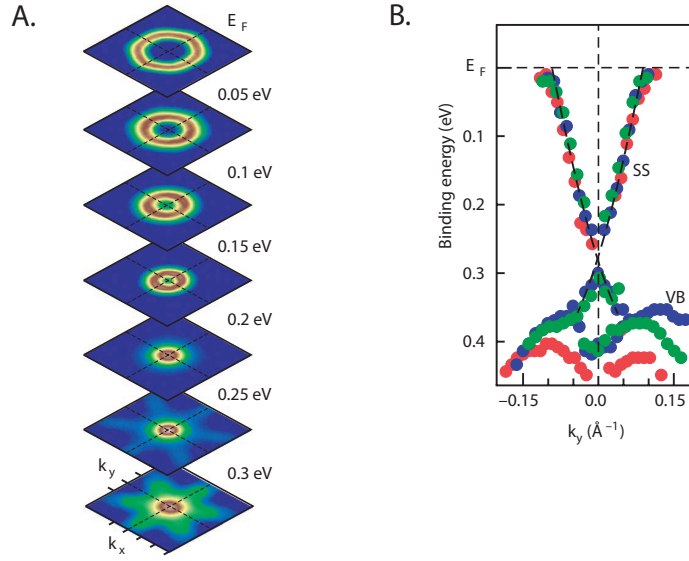


Figure 1.4: A. The cross-section of the Dirac cone in BTS for different binding energies. In the lowest two pictures, traces of the valence band can be seen. B. The Dirac cone for BSTS. The red, blue and green circles correspond to different photon energies of 50, 58 and 70 eV respectively. Figure from [24].

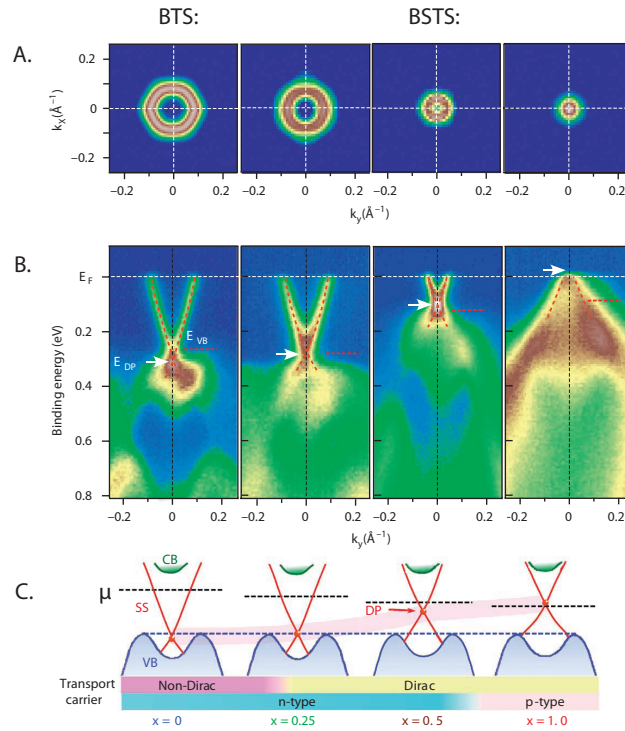


Figure 1.5: The compositions from left to right: (0,1) (BTS), (0.25,1.1), (0.5,1.3) (BSTS) and (1,2). A. The Fermi surface, decreasing in radius with increasing concentration of Sb and Se. B. The dispersion relation; the Dirac cone can be seen to increase with increasing concentration of Sb and Se. C. The schematic dispersion relation, indicating the type of carrier in the surface state. Figure from [24].

called a quintuple layer. Different quintuple layers are connected by the relatively weak Van der Waals bond, while the individual layers in a quintuple layer are connected by a much stronger force.

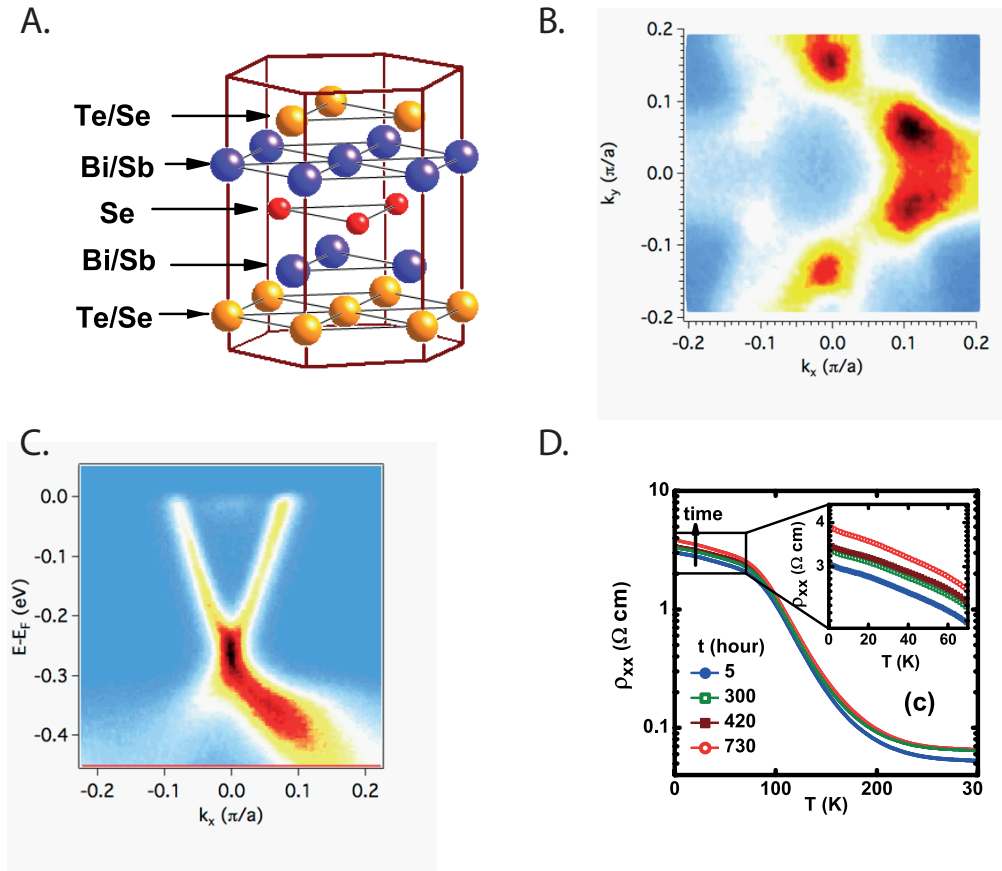


Figure 1.6: A. The structure of BSTS in real space, quintuple layers can be observed. Image from [23] B. A cross-section of the Dirac cone in k -space measured with ARPES. Here, a hexagonal-like structure is visible as well, due to warping effects. C. The typical Dirac cone-like $E(k)$ relationship as measured with ARPES. D. An $R(T)$ measurement of a flake with a thickness of $30 \mu\text{m}$, measured by [23], the resistivity can be seen to increase over time.

It was found that the transport properties of BSTS have a strong time dependence, indicating that the Fermi level of the material shifts in height over time. This fluctuating behaviour asks for a way to control the height of the Fermi level.

1.5 A way to control the Fermi level

One of the ways to control the Fermi level is by using the electric field effect, or ‘gating’. In a simple model one can consider a parallel plate capacitor set-up: two plates separated by a dielectric. When we apply a voltage over the capacitor, charge will accumulate on the surfaces and an electric field will emerge between the plates, equal to $E = \frac{\sigma}{\epsilon}$. When we gate BSTS, we use the same technique to deplete or add charge carriers to the surface state of the BSTS. Remembering that the Fermi energy relates to the charge carrier density via $E_F = \sqrt{4\pi n_s \lambda_{SO}^2}$ we see that we can manipulate the height of the Fermi level by adjusting the amount of charge carriers on the TI surface. In this case, the two parallel plates consist of a substrate of p-doped (conducting) silicon (acting as the first plate) and the BSTS acting as the second. These plates are separated by a 300nm thick layer of silicon dioxide which takes the role of dielectric. Applying a voltage in this way is called back-gating, because the sample is contacted from the back. The set-up is schematically given in figure 1.7. [26]

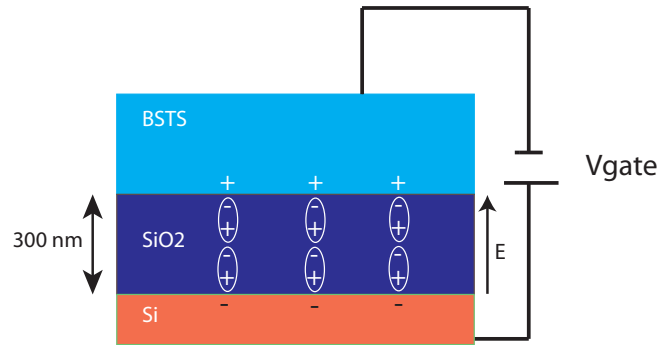


Figure 1.7: The induced electric field as a result of the dipole moments in the dielectric, SiO_2 , positively dopes the BSTS surface state.

Gate experiments on BSTS have also been conducted by [27], by means of an ionic liquid and it was observed that the resistance at low temperatures was modified as can be seen in figure 1.8. This ionic liquid as a mechanism to induce an electric field, however, does not give much control over the applied gate voltage. One cannot continuously vary the voltage, as is the case in the back gate set up.

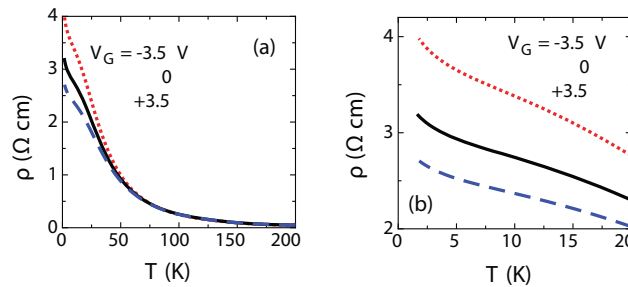


Figure 1.8: Resistivity as a function of temperature with gate voltages of -3.5V, 0V and 3.5V, measured by means of an ionic liquid, taken from [27]. Thickness of the samples is about $180 \mu\text{m}$.

1.6 Current state in the search for the Majorana fermion

Measuring the presence of the Majorana fermion is very indirect. One can do a tunneling conductance measurement, in which the conductance of a barrier is measured as a function of the bias voltage. In the p-wave superconducting case, one would measure the amount of quasiparticles as a function of energy. The Majorana fermion is a quasiparticle excitation in a p-wave superconductor, lying at $E = 0$ (instead of $E < -\Delta$ or $E > \Delta$ as is the case for excitations in an s-wave superconductor). Because of this, a Majorana fermion can emerge as a zero-bias conductance peak (ZBP) in the tunneling conductance spectrum, quantized in units $G(0) = 2 \frac{e^2}{h}$. One group that measured this signature of the Majorana fermion is the Kouwenhoven group from Delft. They used a set-up consisting of 1D indium antimonide nanowires (which features large spin-orbit coupling) in the vicinity of a s-wave superconductor [28], as proposed by different theoretical groups [29, 30, 31, 32], see figure 1.9A. A magnetic field was applied and the tunneling conductance was measured at a temperature as low as $T = 60 \text{ mK}$. It can be seen that a zero-bias conductance peak with an amplitude up to $0.05 \times 2 \frac{e^2}{h}$ emerges between $B = 100 - 400 \text{ mT}$ (figure 1.9C). This is much less than the value of $G(0) = 2 \frac{e^2}{h}$, but this could be the result of thermal broadening. The peak also stays stable for different values of the gate voltage, provided that the Fermi level lies in the gap for non-trivial superconductivity.

Discussions followed, for example Liu et al. [33] did a simulation on a wire with a modest amount of disorder and found that a ZBP also emerges without Majorana fermions. This non-Majorana ZBP was stable under the same range of magnetic fields as measured by [28]. Liu et al. stress that the temperature should be reduced, in order to reduce thermal broadening and to observe a truly quantized ZBP. This would be the evidence that the peak is not the result of some disorder effect.

Another group that has claimed to see signatures of a Majorana fermion is the group of Rokhinson et al. [34], observing it in a semiconductor/superconductor InSb/Nb nanowire junction. Via the AC-Josephson-effect it was concluded that Majorana fermions were found. However it has been suggested that they fitted the wrong type of Bessel functions to their data and by that, their conclusions might be wrong. Convincing evidence for the observation of the MBS should come from a braiding experiment (the exchange of two Majorana fermions), where the wavefunction of the system should change in a different way than it would for normal fermions.

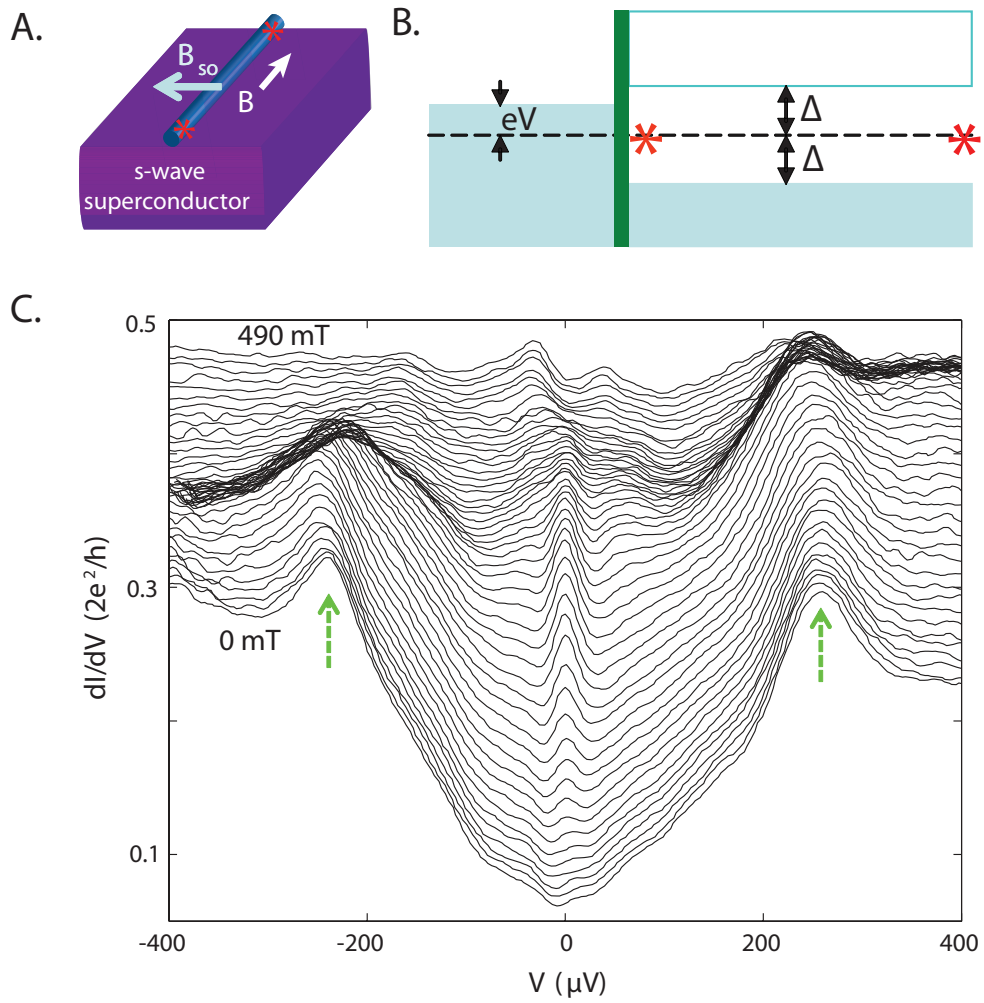


Figure 1.9: A. A schematic of the set-up. By proximity, the wire becomes effectively a p-wave superconductor. B. The tunneling barrier is shown in green, the energy spectrum of the p-wave superconductor on the right. Majorana fermions are shown as the red crosses C. The tunneling conductance at different values for the magnetic field. It is clear that the peak emerges between $B = 100 - 400$ mT. All figures taken from [28].

Chapter 2

Modelling a p-wave superconductor

How can Majorana fermions emerge in a p-wave superconductor? In this chapter an answer will be given to this question. The first two sections will be dedicated to the hunt for Majorana fermions in single material superconductors. The third, fourth and fifth section will be dedicated to finding them in hybrid structures. As mentioned in the last chapter, Majorana fermions will emerge as quasiparticles in superconductors. To study these quasiparticles, we have to go to a microscopic level and make use of the theory that first explained the microscopic mechanism behind superconductivity: Bardeen Cooper Schrieffer (BCS) theory [35, 36].

2.1 Characterizing the excitations of an s-wave superconductor via the BCS Hamiltonian

In this section it will be shown how one can obtain the energy spectrum and form of the broken Cooper pairs, or quasiparticles, in a superconductor [37]. The formalism that is used is second quantization, because it makes calculations easier when dealing with a large number of particles (as is the case in a superconductor). It also gives an intuitive physical picture, as will become apparent in the next sections [38].

In second quantization, the Hamiltonian for an s-wave superconductor is given by:

$$H = \sum_{k,\sigma} E_k \hat{c}_k^\dagger \hat{c}_k - \sum_{k,l} V_{kl} \hat{c}_{-k\downarrow}^\dagger \hat{c}_{k\uparrow}^\dagger \hat{c}_{l\uparrow} \hat{c}_{-l\downarrow}. \quad (2.1)$$

The first term on the right hand side of the equal sign simply describes the total kinetic energy of the electrons (counting them and assigning a certain energy E_k to them) and the second term is the term that pairs electrons with opposite momentum and spin, where V is the attractive pairing potential.

Our goal is to obtain the form and energies of the excitations of the superconductor. We can do this by *diagonalizing* the Hamiltonian, which means that we try to find a way to write this Hamiltonian in which it will not change the state it will work on, i.e. $\hat{H}|\psi_1\rangle = E|\psi_1\rangle$. Clearly, in this form, the second term will change the state it will work on ($\hat{H}|\psi_1\rangle = E|\psi_2\rangle$, $|\psi_1\rangle \neq |\psi_2\rangle$).

The first thing that we have to do is make a *mean field approximation*, in which we assume that quantum fluctuations are small. We write

$$\hat{c}_{-k\downarrow}^\dagger \hat{c}_{k\uparrow}^\dagger = \langle \hat{c}_{-k\downarrow}^\dagger \hat{c}_{k\uparrow}^\dagger \rangle + \delta(\hat{c}_{-k\downarrow}^\dagger \hat{c}_{k\uparrow}^\dagger) \quad (2.2)$$

for both spin directions, where $\langle \hat{c}_{-k\downarrow}^\dagger \hat{c}_{k\uparrow}^\dagger \rangle$ is the expectation value of $\hat{c}_{-k\downarrow}^\dagger \hat{c}_{k\uparrow}^\dagger$ in the ground state, and $\delta(\hat{c}_{-k\downarrow}^\dagger \hat{c}_{k\uparrow}^\dagger)$ are the quantum fluctuations that are assumed to be so

small that $\delta(\hat{c}_{-k\downarrow}^\dagger \hat{c}_{k\uparrow}^\dagger) \delta(\hat{c}_{-k\downarrow}^\dagger \hat{c}_{k\uparrow}^\dagger) = 0$.

If we now write the Hamiltonian in the mean field approximation form, we get a Hamiltonian with terms that are either constants, or have two creation or annihilation operators. Introducing the Nambu spinor representation

$$\Psi_k^\dagger = \begin{pmatrix} \hat{c}_{k\uparrow}^\dagger & \hat{c}_{-k\downarrow} \end{pmatrix}, \Psi_k = \begin{pmatrix} \hat{c}_{k\uparrow} \\ \hat{c}_{-k\downarrow}^\dagger \end{pmatrix}, \quad (2.3)$$

we can write the Hamiltonian in the mean field approximation in the compact form (setting $\xi_k = E_k - \mu$)

$$H = \sum_k \Psi_k^\dagger \begin{pmatrix} \xi_k & -\Delta \\ -\Delta^* & -\xi_k \end{pmatrix} \Psi_k + \sum_k (\xi_k + \Delta b_k). \quad (2.4)$$

In this expression, $\Delta = \sum_l V_{k,l} b_l$, where $b_l = \langle \hat{c}_{-l\downarrow} \hat{c}_{l\uparrow} \rangle$. As can be seen b_l is the expectation value of finding a Cooper pair, so Δ only assumes a non-zero value when Cooper pairs are present in the system, hence only when a material becomes superconducting (when the temperature becomes lower than the critical temperature of the material).

The last step in the process of diagonalization (finding the eigenvalues) is to make a Bogolyubov transformation, in which we introduce new quasiparticle operators that are superpositions of the particle and hole states previously used [39]:

$$\begin{pmatrix} \hat{\alpha}_{k\uparrow} \\ \hat{\alpha}_{-k\downarrow}^\dagger \end{pmatrix} = \begin{pmatrix} u_k^* & v_k \\ -v_k^* & u_k \end{pmatrix} \begin{pmatrix} \hat{c}_{k\uparrow} \\ \hat{c}_{-k\downarrow}^\dagger \end{pmatrix}. \quad (2.5)$$

When we substitute these quasiparticle operators in the Hamiltonian, we are free to choose coefficients u_k and v_k such that we only maintain diagonal terms. It can be shown that this leads to the following expressions for the electron and hole part, respectively:

$$u_k = \sqrt{\frac{1}{2} \left(1 + \frac{\xi_k}{\lambda_k} \right)}, v_k = \sqrt{\frac{1}{2} \left(1 - \frac{\xi_k}{\lambda_k} \right)}, \text{ where } \lambda_k = \sqrt{\xi_k^2 + \Delta^2}. \quad (2.6)$$

The diagonalized BCS mean field Hamiltonian becomes:

$$H = E_0 + \sum_{k\sigma} \lambda_k \left(\hat{\alpha}_{k\sigma}^\dagger \hat{\alpha}_{k\sigma} + \hat{\alpha}_{-k\sigma}^\dagger \hat{\alpha}_{-k\sigma} \right), \quad (2.7)$$

where $E_0 = \sum_k \xi_k - \lambda_k + \Delta b_k$.

We have now diagonalized our Hamiltonian and thus found the eigenvalues of the BCS Hamiltonian, be it in a mean field approximation. Looking at the operators that diagonalize this Hamiltonian, we see that these quasiparticles are basically superpositions of an electron and a hole and have the form (up to the coefficients): $\hat{\alpha}_{k\uparrow} = \hat{c}_{k\uparrow} + \hat{c}_{-k\downarrow}^\dagger$. The question is: can these particles be their own anti-particles? No, because even though we can choose $k = 0$, then $\hat{\alpha}_{0\uparrow} = \hat{c}_{0\uparrow} + \hat{c}_{0\downarrow}^\dagger$ and $\hat{\alpha}_{0\uparrow}^\dagger = \hat{c}_{0\uparrow}^\dagger + \hat{c}_{0\downarrow} \neq \hat{\alpha}_{0\uparrow}$, hence there is still a spin index that keeps us from having Majorana fermions [8]. Knowing this, it is natural for us to look for Majorana fermions in systems where electrons pair with equal spin, so the spin index is not relevant anymore. This type of superconductor is the ‘p-wave’ superconductor, let us proceed and see if this is true if we do the same analysis for a Hamiltonian of a p-wave superconductor.

2.2 Majorana fermions in a p-wave superconductor

In a p-wave superconductor the pairing of electrons is different to the s-wave case, as it pairs spins of the same direction, for example (\mathbf{k}, \uparrow) and $(-\mathbf{k}, \uparrow)$. We know that for fermions, the total wavefunction of a Cooper pair has to be anti-symmetric and this can only be the case if an odd number of components of the total wavefunction is anti-symmetric. In our case the total wavefunction of the condensate has two components: the spin component and the orbital component. In the p-wave case, the spin component of the wavefunction is symmetric (equal spin pairing), hence the orbital component of the wavefunction should be anti-symmetric, which will be shown in this section. In the next section we will investigate what the energy and form of the excitations in a p-wave superconductor will be.

The Hamiltonian that describes a p-wave superconductor is given by [40] :

$$H = \sum_k E_k \hat{c}_k^\dagger \hat{c}_k - \sum_{k,l} V_{kl} (k_x - ik_y) (l_x + il_y) \hat{c}_k^\dagger \hat{c}_{-k}^\dagger \hat{c}_{-l} \hat{c}_l. \quad (2.8)$$

We can immediately see an important difference with the s-wave Hamiltonian: in the interaction term, the spin degree of freedom has been dropped. This is because it is unnecessary when considering pairing of equal spin. Also the factors in front of the creation and annihilation operators in the pairing term are different, these can be written:

$$k_x - ik_y = |\mathbf{k}| e^{i\theta_k}, \quad \theta_k \equiv \arctan\left(\frac{k_y}{k_x}\right) \quad (2.9)$$

We will follow the procedure of the previous section, i.e. diagonalizing via a mean field approximation and a Bogolyubov transformation. In the mean field approximation, we will take

$$\hat{c}_{-k}^\dagger \hat{c}_k^\dagger = \langle \hat{c}_{-k}^\dagger \hat{c}_k^\dagger \rangle + \delta(\hat{c}_{-k}^\dagger \hat{c}_k^\dagger), \quad (2.10)$$

note again the absence of the spin indices. Now we can just copy the steps from the last section: using the Nambu notation 2.3 (without the spin indices) and writing the Hamiltonian in the mean field approximation:

$$H = \sum_k \Psi_k^\dagger \begin{pmatrix} \xi_k & -\Delta(\mathbf{k}) \\ -\Delta^*(\mathbf{k}) & -\xi_k \end{pmatrix} \Psi_k + \sum_k (\xi_k + \Delta b_k). \quad (2.11)$$

In this equation, $\Delta(\mathbf{k}) = \Delta |\mathbf{k}| e^{i\theta_k}$, where $\Delta = \sum_l V_{k,l} |\mathbf{l}| e^{i\theta_l} b_l$. In this case $b_l = \langle \hat{c}_{-l}^\dagger \hat{c}_l^\dagger \rangle$.

We can see that there is a difference in the order parameter $\Delta(\mathbf{k})$ between an s-wave and a p-wave superconductor. If we plot the real part of the directional dependence of the p-wave superconductor, we get a shape that resembles the p-orbital wavefunction of the hydrogen atom as can be seen in figure 2.1. This is the antisymmetric orbital part of the wavefunction.

Let us now perform a Bogolyubov transformation. For the spinless superconductor, the new quasiparticles become:

$$\begin{pmatrix} \hat{\alpha}_k \\ \hat{\alpha}_{-k}^\dagger \end{pmatrix} = \begin{pmatrix} u_k^* & v_k \\ -v_k^* & u_k \end{pmatrix} \begin{pmatrix} \hat{c}_k \\ \hat{c}_{-k}^\dagger \end{pmatrix}. \quad (2.12)$$

Again, we are free to choose the coefficients such that we only maintain diagonal elements:

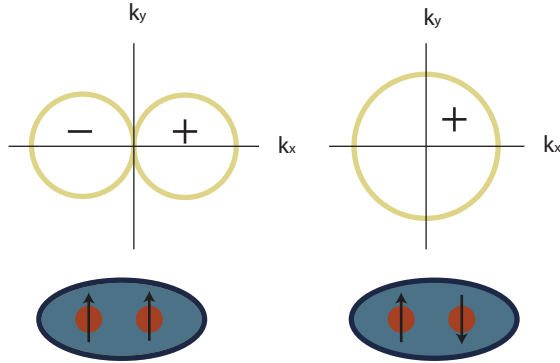


Figure 2.1: Left: the shape of the order parameter (real part) in k-space for a p-wave superconductor that pairs electrons of equal spin direction (below). Right: the shape of the s-wave parameter, isotropic in k-space, pairing electrons of opposite spin directions

$$u_k = \sqrt{\frac{1}{2} \left(1 + \frac{\xi_k}{\lambda_k} \right)} e^{i\theta_k}, \quad v_k = \sqrt{\frac{1}{2} \left(1 - \frac{\xi_k}{\lambda_k} \right)}, \quad \lambda_k = \sqrt{\xi_k^2 + |\Delta|^2}, \quad (2.13)$$

in this way the Hamiltonian is diagonalized. We already see that there is no spin index in these operators. Let us look at these quasiparticles and write out the upper operator in 2.12:

$$\hat{\alpha}_k = u_k^* \hat{c}_k + v_k \hat{c}_{-k}^\dagger. \quad (2.14)$$

The corresponding anti-commutation relation of these quasiparticles reveal fermionic behaviour:

$$[\hat{\alpha}_k, \hat{\alpha}_{k'}^\dagger]_+ = \delta_{k,k'}, \quad [\hat{\alpha}_k^\dagger, \hat{\alpha}_{k'}^\dagger]_+ = [\hat{\alpha}_k, \hat{\alpha}_{k'}]_+ = 0. \quad (2.15)$$

This means that these particles are fermions. If we now only consider the case $k = 0$, then $\xi_{k=0} = 0$ (if $\mu = 0$) and we take $\theta_k = 0$, then $u_{k=0} = v_{k=0}$ and this quasiparticle annihilation operator is exactly equal to its complex conjugate (i.e. $\hat{\alpha}_{k=0} = \hat{\alpha}_{k=0}^\dagger$). These quasi-particles have a rather strange anti-commutation relation:

$$[\hat{\alpha}_0, \hat{\alpha}_0^\dagger]_+ = [\hat{\alpha}_0^\dagger, \hat{\alpha}_0^\dagger]_+ = [\hat{\alpha}_0, \hat{\alpha}_0]_+ = 2. \quad (2.16)$$

Nevertheless, we call these particles fermions. This means that an excitation in a p-wave superconductor can under certain circumstances (at zero energy) be a fermionic quasiparticle that is indeed its own anti-particle!

In nature, superconductors with an intrinsic p-wave pairing symmetry are scarce, it is predicted to occur in the material Sr_2TiO_4 , but with so few impurities that it is not yet experimentally realizable [41]. This is why we have to combine different materials and rely on the proximity effect of the superconducting condensate: when a material is brought close to an s-wave superconductor, the condensate wavefunction will extend into the other material and change its pairing symmetry. In the next section, it will be shown how to transform the s-wave pairing symmetry into p-wave by using a topological insulator and eventually other spin orbit coupled materials. We will start with the standard recipe, a TI + s-wave superconductor, and later on substituting a TI for a simpler, better known material with spin orbit coupling.

2.3 A conventional s-wave superconductor in proximity to a topological insulator

In the last chapter the topological insulator was introduced: materials that are insulating in the bulk and conducting on the surface. This is due to the fact that they are insulators with a large spin-orbit coupling (SOC). The spin-orbit coupled bands connect the valence and the conduction bands that are gapped. This gapped region can be described by a model Hamiltonian that only takes into account the chemical potential and Rashba SOC. The Rashba SOC term comes from the Pauli equation [42], which is the non-relativistic limit of the Dirac equation and has the form (in first quantization) [43]:

$$H_{SO} = \lambda (\boldsymbol{\sigma} \times \mathbf{k}) \cdot \hat{\mathbf{z}}, \quad (2.17)$$

where λ is the strength of the spin-orbit coupling (proportional to the electric field, that emerges as a result of the breaking of inversion symmetry) and $\boldsymbol{\sigma}$ denotes the Pauli spin matrices. If we now write the model Hamiltonian for the topological insulator, we get:

$$H = \sum_k \Psi_k^\dagger \mathcal{H} \Psi_k = \sum_k \Psi_k^\dagger \begin{pmatrix} \mu & i\lambda|\mathbf{k}|e^{-i\theta_k} \\ -i\lambda|\mathbf{k}|e^{i\theta_k} & \mu \end{pmatrix} \Psi_k, \quad (2.18)$$

where in this case:

$$\Psi_k^\dagger = \left(\hat{c}_{k\uparrow}^\dagger, \hat{c}_{k\downarrow}^\dagger \right), \quad \Psi_k = \begin{pmatrix} \hat{c}_{k\uparrow} \\ \hat{c}_{k\downarrow} \end{pmatrix}. \quad (2.19)$$

It can be seen that the spin-orbit coupling operators change the state from spin down to spin up and vice versa. What we now want to do is find the eigenvalues for this system, which we will do by finding a basis, $\tilde{\Psi}_k$ that diagonalizes the Hamiltonian, like we did in the last section. In this case, diagonalization can be done by calculating the eigenvalues of the matrix \mathcal{H} , κ , by solving $|\mathcal{H} - \mathbf{I}\kappa| = 0$, we find $\kappa = -\mu \pm \lambda|\mathbf{k}|$. The next step is to find the corresponding eigenvectors via $(\mathcal{H} - \mathbf{I}\kappa)\mathbf{v} = 0$. Now we know that the matrix \mathcal{H} is diagonalized via $P^\dagger \mathcal{H} P$, where $P = (\mathbf{v}_1, \mathbf{v}_2)$, i.e. the matrix with the eigenvectors as columns.

Since we know that $P^\dagger \mathcal{H} P$ is a diagonal matrix, we know that $\sum_k \tilde{\Psi}_k^\dagger P^\dagger \mathcal{H} P \tilde{\Psi}_k$ is our Hamiltonian in the diagonalized form. This Hamiltonian should be equal to $\sum_k \Psi_k^\dagger \mathcal{H} \Psi_k$, so we can find the transformed basis via:

$$P^\dagger \Psi_k = \tilde{\Psi}_k, \quad (2.20)$$

which gives:

$$\tilde{\Psi}_k = \begin{pmatrix} \hat{c}_{k+} \\ \hat{c}_{k-} \end{pmatrix} = \frac{1}{\sqrt{2}} \begin{pmatrix} \hat{c}_{k\downarrow} - ie^{i\theta_k} \hat{c}_{k\uparrow} \\ \hat{c}_{k\downarrow} + ie^{i\theta_k} \hat{c}_{k\uparrow} \end{pmatrix}. \quad (2.21)$$

Note that the new basis, $\hat{c}_{k\pm}$, carries a different kind of spin-index \pm in the operators, this is called the helicity. We can make this helicity-transformation because the spin of the electron is coupled to the value of \mathbf{k} . Intuitively, one can understand this by imagining oneself ‘sitting’ on the electron state in the Dirac cone and turning with the angle θ ; the spin direction of the electron state will, from this perspective, maintain the same direction throughout the entire turn. This transformation is illustrated in figure 2.2, where the dispersion relation of the 2D surface states of the topological insulator is illustrated.

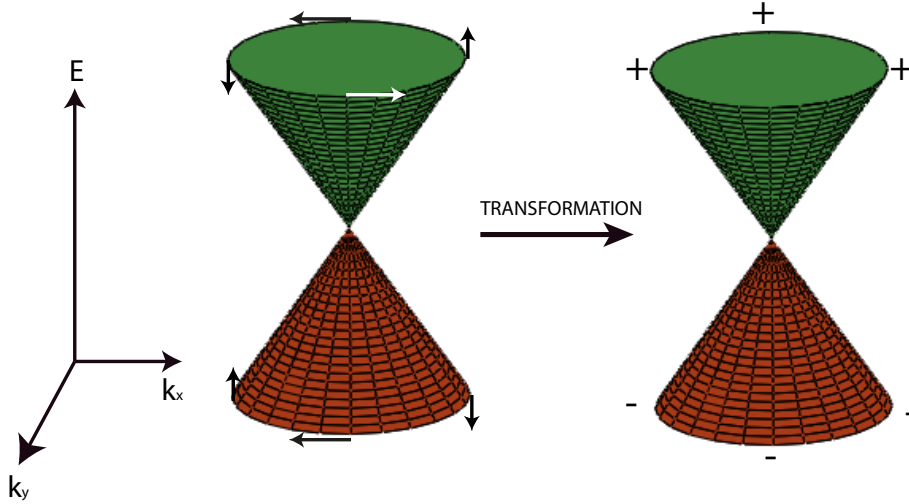


Figure 2.2: Spin is included in left cone, helicity index in right cone.

Let us now look at what happens if we bring the TI in contact with a superconductor [4], assuming a fully transparent interface between the two materials. Due to the proximity effect as mentioned earlier, Cooper pairs will tunnel to the TI, and part of the TI will become superconducting [44]. The corresponding pairing symmetry of the condensate in the TI can be obtained by studying the Hamiltonian. We know from the previous chapter that it is appropriate to use the Nambu particle-hole basis when dealing with superconductors, so we have to use a basis that combines the Nambu basis for superconductivity and the spin basis for spin-orbit coupling:

$$\Psi_k^\dagger = \left(\hat{c}_{k\uparrow}^\dagger, \hat{c}_{k\downarrow}^\dagger, \hat{c}_{-k\uparrow}, \hat{c}_{-k\downarrow} \right). \quad (2.22)$$

We include the terms that describe s-wave superconductivity in a mean field form in the Hamiltonian, just like we did in equation 2.4, mixing particle and hole operators. The total Hamiltonian becomes ¹:

$$H = \sum_k \Psi_k^\dagger \begin{pmatrix} \mu & i\lambda|\mathbf{k}|e^{-i\theta_k} & 0 & \Delta \\ -i\lambda|\mathbf{k}|e^{i\theta_k} & \mu & -\Delta & 0 \\ 0 & -\Delta & -\mu & -i\lambda|\mathbf{k}|e^{i\theta_k} \\ \Delta & 0 & i\lambda|\mathbf{k}|e^{-i\theta_k} & -\mu \end{pmatrix} \Psi_k. \quad (2.23)$$

If we now substitute the basis that we obtained after diagonalizing the Hamiltonian for the TI:

$$\Psi_k^\dagger = \left(\hat{c}_{k\uparrow}^\dagger, \hat{c}_{k\downarrow}^\dagger, \hat{c}_{-k\uparrow}, \hat{c}_{-k\downarrow} \right) \rightarrow \tilde{\Psi}_k^\dagger = \left(\hat{c}_{k+}^\dagger, \hat{c}_{k-}^\dagger, \hat{c}_{-k+}, \hat{c}_{-k-} \right), \quad (2.24)$$

we arrive at the following Hamiltonian:

$$H = \sum_k \tilde{\Psi}_k^\dagger \begin{pmatrix} \mu - \lambda|\mathbf{k}| & 0 & \Delta(\mathbf{k}) & 0 \\ 0 & \mu + \lambda|\mathbf{k}| & 0 & -\Delta(\mathbf{k}) \\ -\Delta^*(\mathbf{k}) & 0 & -\mu + \lambda|\mathbf{k}| & 0 \\ 0 & \Delta^*(\mathbf{k}) & 0 & -\mu - \lambda|\mathbf{k}| \end{pmatrix} \tilde{\Psi}_k. \quad (2.25)$$

¹This term should be multiplied by a factor $\frac{1}{2}$, to avoid counting the particles double (electrons and holes). I leave this factor out to avoid cumbersome notation.

In this Hamiltonian we see that the pairing terms have the operator form $\hat{c}_{-k} + \hat{c}_{k+}$, i.e. it pairs carriers with equal helicity. Here $\Delta(\mathbf{k}) = \Delta i e^{i\theta_k} = \Delta e^{i\frac{\pi}{2}} e^{i\theta_k} = \Delta e^{i(\theta_k + \frac{\pi}{2})}$, this means that an s-wave superconductor in proximity with a TI is effectively indeed a p-wave superconductor! The equal helicity-index pairing is visualised in figure 2.3, where the cross-section of the Dirac cone is shown.

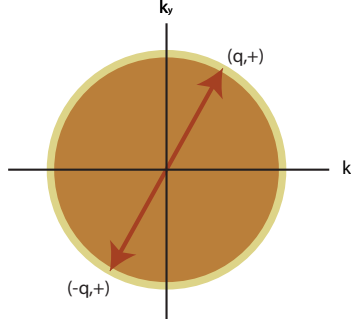


Figure 2.3: A cross section of the Dirac cone, where carriers with equal helicity pair up.

2.4 The s-wave superconductor in proximity to a metal with spin-orbit coupling

Since spin-orbit coupling seems to be the key ingredient for p-wave superconductivity (which is the key ingredient for Majorana's), it will be interesting to study systems that consist of a metal with SOC on top of an s-wave superconductor. The Hamiltonian of this system features a free term, next to the SOC and the BCS-term. This free term originates from the fact that a metal is a conductor; there are electrons in a metal that can move around freely (although they are still spin-orbit coupled).

Expected is that the Hamiltonian of the system shows, when the kinetic part is diagonalized, a mix of p- and s-wave superconductivity. The s-wave component will originate from the free term in the Hamiltonian. If this is the case, we expect that the term that describes p-wave superconductivity will in some way be proportional to the strength of the SOC. In this mixing-case, the wavefunction of the condensate in k-space will be a superposition of p- and s-wave components as illustrated in figure 2.4.

A workable metallic material that has this property of SOC is gold. The SOC in gold originates from the fact that gold is a relatively heavy element, through which the electrons experience an electric field when inversion symmetry is broken (i.e. at the surface) [45]. This surface (in the (111)-direction) state spin splitting has been measured by LaShell et al. [46] with ARPES. In figure 2.5 this spin-splitting is shown. Also from a practical point of view, gold is a good material to work with. In the laboratory, there is lots of experience with the deposition of gold.

In this section it will be investigated whether or not it is possible to have mixed superconductivity, starting with proposing a model Hamiltonian for a metal with SOC and later on adding superconductivity.

2.4.1 Model Hamiltonian for a metal with spin-orbit coupling

The main difference between a topological insulator and a metal with spin-orbit coupling is that the metal is conducting, hence a free term should be introduced. Free electrons

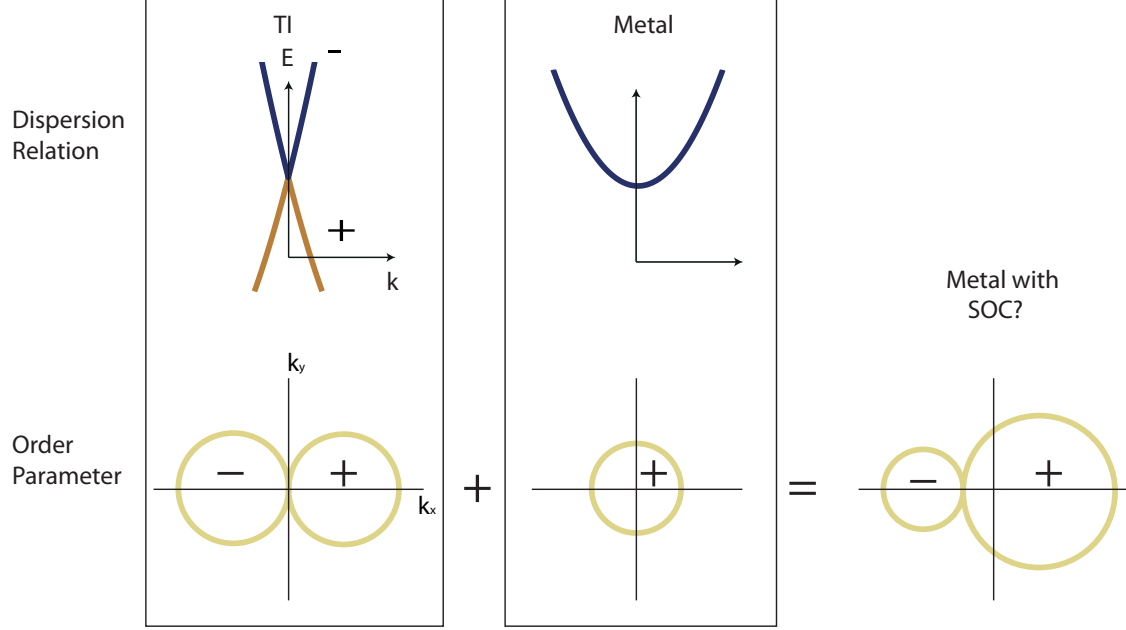


Figure 2.4: Mixing of p-wave (left, corresponding to the TI dispersion relation) and s-wave (corresponding to the metal dispersion relation) components of the wavefunction of the condensate might give a superposition.

have an energy of $E_k = \frac{\hbar^2|\mathbf{k}|^2}{2m} = \alpha k^2$, i.e. a quadratic dispersion relation. This appears in second quantization in the Hamiltonian as:

$$H^{free} = \sum_{k,\sigma} \alpha k^2 \hat{c}_{k\sigma}^\dagger \hat{c}_{k\sigma} - \alpha k^2 \hat{c}_{-k\sigma} \hat{c}_{-k\sigma}^\dagger. \quad (2.26)$$

This expression simply counts the electrons (holes) and assigns an energy αk^2 ($-\alpha k^2$) to them, and therefore appears on the diagonal of the Hamiltonian matrix.

We add this expression to the Hamiltonian of the topological insulator to get:

$$H^{Au} = \sum_k \Psi_k^\dagger \begin{pmatrix} \mu + \alpha k^2 & i\lambda|\mathbf{k}|e^{-i\theta_k} \\ -i\lambda|\mathbf{k}|e^{i\theta_k} & \mu + \alpha k^2 \end{pmatrix} \Psi_k, \quad (2.27)$$

in the basis given by 2.19. We can now repeat the steps taken in the last section to

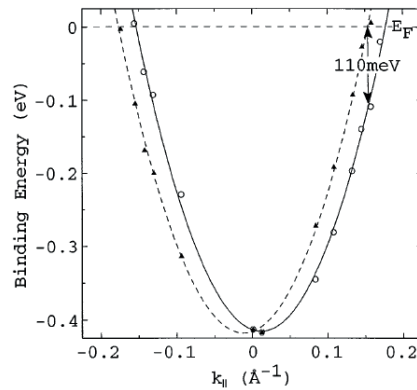


Figure 2.5: The result of an ARPES measurement on the (111)-surface of gold. The bands are split due to spin-orbit coupling.

diagonalize this Hamiltonian, and the peculiar result is that the whole diagonalization process is the same except for the eigenvalues: $\kappa = -\mu - \alpha k^2 \pm \lambda|\mathbf{k}|$. The new basis $\tilde{\Psi}_k$ that diagonalizes this Hamiltonian is given by 2.21.

Writing this in diagonalized form gives us the dispersion relation:

$$H^{Au} = \sum_k \tilde{\Psi}_k^\dagger \begin{pmatrix} \mu + \alpha k^2 - \lambda|\mathbf{k}| & 0 \\ 0 & \mu + \alpha k^2 + \lambda|\mathbf{k}| \end{pmatrix} \tilde{\Psi}_k. \quad (2.28)$$

The dispersion relation, for different strengths of spin-orbit coupling is plotted in figure 2.6.

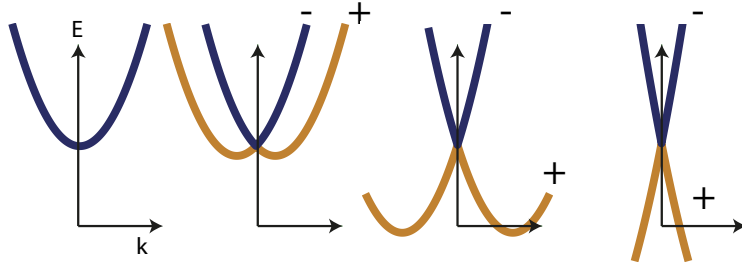


Figure 2.6: Spin orbit coupling is increased when going from left to right.

2.4.2 A metal with spin-orbit coupling and the s-wave superconductor

Motivated by the idea of Majorana fermions, let us once again switch on superconductivity, again assuming a fully transparent barrier. As in the case of the TI, part of the metal will also become superconducting. This can effectively be described by a Hamiltonian that somewhat resembles 2.23, up to the quadratic terms on the diagonal:

$$H = \sum_k \Psi_k^\dagger \begin{pmatrix} \mu + \alpha k^2 & i\lambda|\mathbf{k}|e^{-i\theta_k} & 0 & \Delta \\ -i\lambda|\mathbf{k}|e^{i\theta_k} & \mu + \alpha k^2 & -\Delta & 0 \\ 0 & -\Delta & -\mu - \alpha k^2 & -i\lambda|\mathbf{k}|e^{i\theta_k} \\ \Delta & 0 & i\lambda|\mathbf{k}|e^{-i\theta_k} & -\mu - \alpha k^2 \end{pmatrix} \Psi_k. \quad (2.29)$$

Now we make the same substitution as in 2.24 and we see that the Hamiltonian has almost the same form as 2.25:

$$H = \sum_k \tilde{\Psi}_k^\dagger \begin{pmatrix} \mu + \alpha k^2 - \lambda|\mathbf{k}| & 0 & \Delta(\mathbf{k}) & 0 \\ 0 & \mu + \alpha k^2 + \lambda|\mathbf{k}| & 0 & -\Delta(\mathbf{k}) \\ -\Delta^*(\mathbf{k}) & 0 & -\mu - \alpha k^2 + \lambda|\mathbf{k}| & 0 \\ 0 & \Delta^*(\mathbf{k}) & 0 & -\mu - \alpha k^2 - \lambda|\mathbf{k}| \end{pmatrix} \tilde{\Psi}_k. \quad (2.30)$$

The peculiarity of this result is striking: this Hamiltonian only carries a p-wave superconductivity component, $\Delta(\mathbf{k})$, no s-wave. It seems as if the system effectively behaves as a p-wave superconductor once the spin-orbit coupling strength, λ , however small, assumes a non-zero value. So even in the case of infinitely weak spin-orbit coupling, the system is fully p-wave, without even a trace of a s-wave component. This makes sense when considering that there is no mechanism that gives the electrons a preferred spin direction in the free case (without SOC). When SOC is turned on, the electrons get a preferred spin direction, however small the strength of this coupling, because there is no force to compete with.

2.5 Majorana fermions?

We do now have a system that can have p-wave superconductivity, but the question is if it will feature Majorana fermions. For this we have to consider the dispersion relation, given in figure 2.7.

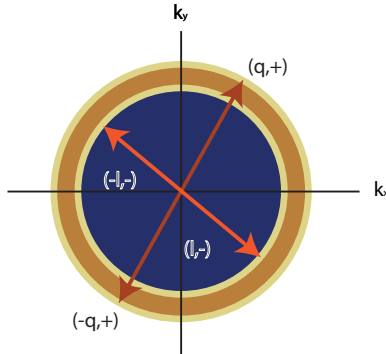


Figure 2.7: Pairing of electrons, analogous to the topological insulator case, where in the case of a metal with SOC the outer branches of the spin-orbit coupled, quadratic bands still play a role.

We see that the condensate will feature a degeneracy in the spin helicity, pairing spin helicity - and +, resulting again in s-wave superconductivity. The system can be converted to p-wave superconductivity by applying a magnetic field (breaking time reversal symmetry and introducing a so called Zeeman gap) and tuning the Fermi level in the right range, as shown in figure 2.8, [8, 7]. When the magnetic field is large enough, i.e. $V_B > \Delta$ (where V_B is the energy gap induced by the magnetic field, the Zeeman gap), the upper band can be neglected and the superconductivity is p-wave. However this applied magnetic field also couples to the spin of the electrons, changing it by an angle θ , which introduces an s-wave component in the superconductivity as shown in Ref. [47]. So in the case that the magnetic field becomes large as compared to the spin-orbit coupling, the s-wave component of the superconductivity prevails, and Majorana bound states will not emerge.

A set-up to test this would resemble the one used by Kouwenhoven [28], in this case the nanowire would be made of gold instead of a semiconductor.

2.6 Recommendations

This analysis has been done for a hybrid system with a fully transparent barrier. In reality though, barriers between different materials feature a lack of transparency, which can be modeled by introducing a delta function potential at the interface of the two materials. For an analysis on these more realistic systems we refer to a review paper by Tanaka et al. [48]. Also a paper was published by Potter during the writing of this thesis in which they investigate the possibility of Majorana fermions in Au(111)-surface states [49].

2.7 The importance of gating

From figure 2.8 we observe that having the Fermi level at the appropriate height is one of the factors that is of high importance in the view of Majorana fermions. The height of the Fermi level can be manipulated by applying a gate voltage, as shown in the introduction.

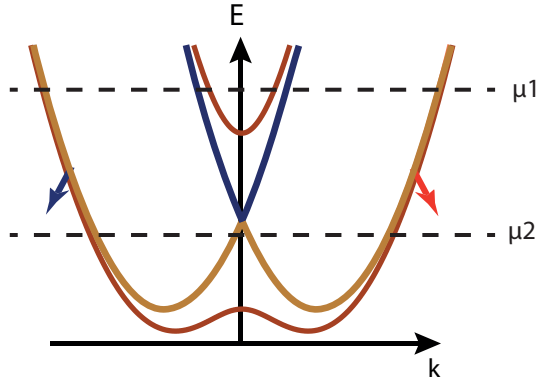


Figure 2.8: The change in the dispersion relation when a magnetic field is applied, brown and blue show the bands when SOC is the only mechanism coupling to spin, the red curves show the bands when the field is switched on. Here μ_1 shows the level of the chemical potential to obtain a topologically nontrivial system, crossing the + and - bands, thus preventing Majorana fermions. μ_2 is tuned in the Zeeman gap, crossing only one of the helicity spin bands, the appropriate level for Majorana fermions.

Tuning the Fermi level is also important in heterostructures with topological insulators, because although the level already lies in the region appropriate for topologically non-trivial superconductivity, one also wants to be able to control other material parameters that depend on the position of the Fermi level in the Dirac cone. The next chapters will be dedicated to the experimental realization of a topological insulator, BSTS, with a variable Fermi level.

Chapter 3

Set-up and sample preparation

Preparing thin films of BSTS for gate measurements can be a challenging task, because leakage currents need to be avoided and a small and delicate sample must be conserved and not be blown up. In the first part of this chapter it is shown how to prepare a sample without having leakage currents. In the second part the measurement set-up is introduced.

3.1 Applying BSTS to the substrate

Workable thin film samples of BSTS were made by applying them to a substrate. The substrate that was used consisted of a silicon layer (1 by 1 *cm*, thickness of 1*mm*) with a 300 nm layer of SiO₂ on top. The silicon layer is p-doped with boron to obtain a low resistivity (0.010 - 0.025 Ωcm). Before the BSTS film can be applied, it must be ensured that the substrate is very clean, otherwise the experiment can be contaminated. The cleaning is done by submerging the substrate in an acetone bath, in a glass beaker, after which it is ultrasonically cleaned for 4 minutes. To make sure no traces of the acetone will be left on the substrate, the same treatment is applied in an ethanol bath for 3 minutes after which the substrate is dried with nitrogen. Now that the substrate is thoroughly cleaned, the BSTS film can be applied. To obtain a thin film of BSTS from a crystal, a method called ‘micromechanical exfoliation’ or the ‘scotch tape method’ has been used. Thin layers of the crystal were peeled off with scotch tape and applied onto the substrate. This way of obtaining thin films from a crystal was inspired by experiments done on graphene [50]. With this method, quintuple layers of BSTS are exfoliated due to the weak Van der Waals force that binds them. Because of this weak binding force, one does not need much pressure in the process of applying the flake to the substrate. This can be done for example by laying the scotch tape with the cleaved crystal parts on the SiO₂-surface and pressing it with the least force possible, for example by letting the tip of a pair of tweezers rest on it, while moving the tweezers around on the surface. This gentle treatment is needed in order to keep the SiO₂ layer in good condition. After this, the scotch tape has to be removed from the sample as slowly and under the smallest angle as possible (see figure 3.1), to ensure that the quintuple layers be neatly exfoliated and smooth flakes (with high mobility surface states) are obtained.

3.2 Preparing the contacts by photolithography

Now that the BSTS is deposited on the substrate, the essential part of our to-be-gated sample is ready. But one also needs to contact the flake in order to evoke currents and to

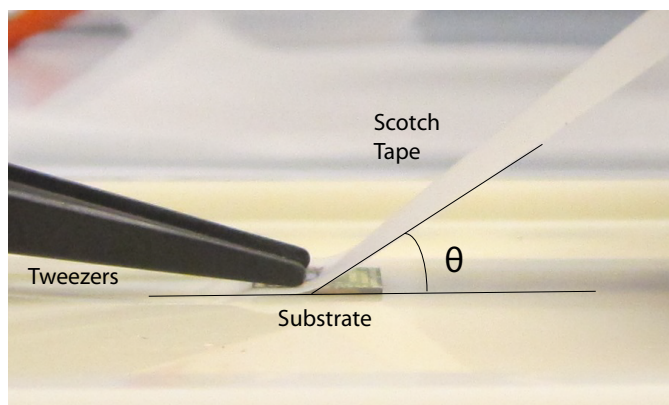


Figure 3.1: The last step in the process of mechanical exfoliation. The angle θ should be kept as small as possible while removing the scotch tape. It also helps to do this as slow as possible (take 2 minutes to remove the tape).

apply a gate voltage. For this we prepare gold contacts on the flake, from which we will make contact to the measurement apparatus by a process called wirebonding.

In order to make the gold contacts, one first has to define them. This is done by a process called photolithography. A liquid called photoresist is deposited on the surface of the sample by spin coating. The photoresist that is used is one with a thickness of $1.2 \mu\text{m}$ and the spinning time is 45 seconds, at a speed of 6000 rounds per minute. After the coating has been applied, the sample is baked out for one minute at 373 K. With UV exposure for 8 seconds and a mask, the structure of the contacts is defined and the photoresist structure is ready when the developer washes away the parts where the gold is going to be deposited (for positive resist). This washing process consists of 1 minute submersion in developer and an additional two times half a minute in demiwater (each time in a new glass beaker), to clean off the developer.

In the next step, gold is being deposited in a Perkin Elmer sputtering system to make contacts to the flake. The process starts with argon etching for 5 to 15 seconds (at a power of 150 W), a really short time because etching reduces the thickness of the photoresist and the layer of photoresist needs to be as thick as possible after the deposition (to ensure lift off). After this, a thin layer of titanium is deposited for 15 seconds, at a power of 150 W , this corresponds to a layer of 2 nm. The titanium acts as a ‘glue’ between the substrate and the gold. Finally, the 60 nm layer of gold is deposited, for 1.5 minutes at 150 W . The last step of the deposition process is ‘lift off’; the substrate is submerged in acetone, for a time varying from 3 to 24 hours, to remove the excess gold as defined by the photoresist. The acetone is cleaned off by submersion in ethanol for one minute, after which the sample is dried with nitrogen. A schematic of the flake with the gold contacts is shown in figure 3.2 .

3.3 Preparing the contacts by electron beam lithography

Another way one can define a pattern for the gold deposition is by electron-beam (ebeam) lithography. Electrons have a much smaller wavelength than photons, therefore we can obtain much smaller resolutions than photolithography and thus design smaller structures like Hall-bars. Instead of photoresist a chemical called ‘polymethylmethacrylate’ (PMMA) is used and instead of a mask to define the structures, software is used, which leaves more freedom in defining structures. An image of a flake with contacts defined by ebeam lithography, made with a scanning electron microscope is shown in figure 3.3. For

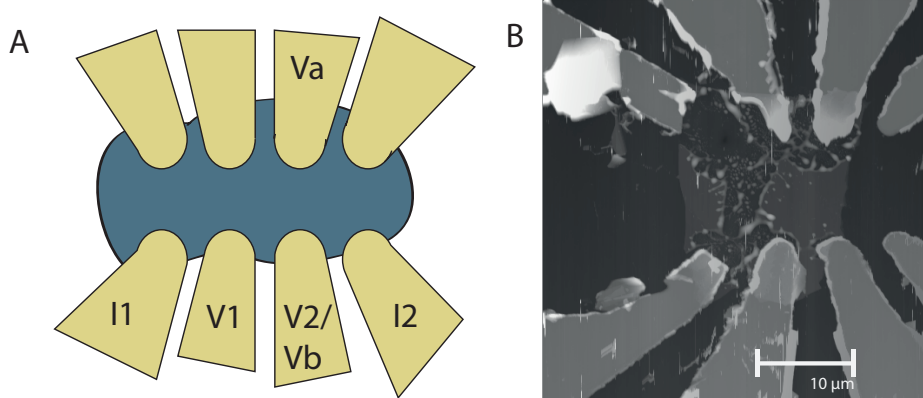


Figure 3.2: A. A flake (blue) with gold contacts made by photolithography. A current is sent between the outer two contacts (I1 and I2), the corresponding voltage drop is measured over the two middle contacts (V1 and V2). When a magnetic field is applied, the Hall-resistance is measured between Va and Vb. Although this is not a well-defined Hall bar, an approximate (order of magnitude) and trend in the carrier density and mobility can be measured. B. What a flake looks like when blown up. This can happen when for instance a current runs through the flake that is too high, or by static discharge. It is the sad fate of all the measured flakes.

information on the specific parameters used in the ebeam designs, see the Appendix.

Photolithography is the main technique that is used for contacting flakes in this project, this has mainly to do with time; the e-beam lithography machine is intensively used so making a Hall bar (which needs multiple ebeam-steps) can easily take a month, if not more. Ebeam lithography is instead used to make contacts to flakes (which takes only one ebeam-step, much less time than making a Hall bar), because with this technique it is possible to contact multiple flakes on one sample.

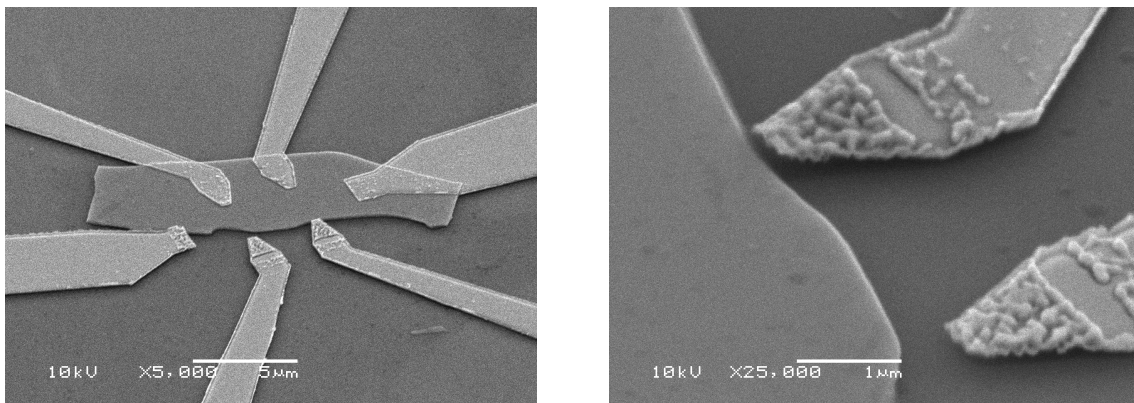


Figure 3.3: A flake with gold contacts defined by ebeam lithography. Right: The contacts do not reach the flake due to line-out problems. These problems occurred with some of the flakes that were unusually small.

3.4 Back-gate contact and the connection to the measurement apparatus

The positive side of the gate is connected to the p++ -doped silicon, the negative side will be connected to the top of the sample. It is important in a gate experiment that the applied voltage over the sample will not induce a current (leakage current). Two possibilities for the origin of a leakage current will be given:

1. The current leaks away through the SiO_2 (figure 3.4A).
2. The current leaks away from the silicon backside to the measurement apparatus (puck) that is connected to ground (figure 3.4B);

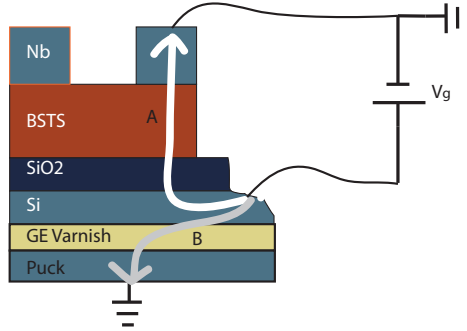


Figure 3.4: Two different possibilities for a leakage current, Ge Varnish is the glue that is used to attach the sample to the puck

The solution to the first problem is to be as gentle as possible in the treatment of the SiO_2 layer. This means that flake deposition, as is already reported, should be done with the least amount of pressure possible. Another critical step is the wirebonding, the process in which the gold contacts are connected to the measurement puck. The wirebonder uses ultrasonic soldering to connect the wire to the gold pads, thereby pushing the wire against the gold. In order not to damage the SiO_2 , one must make sure that this push happens with the least amount of force, and the soldering with the least amount of power, but still enough force and power that the wire will still be connected to the gold. Experiments were done to determine the ideal setting for the force and power and these were found to be: $power = 2$, $time = 10$, $mass_{tip} = 28\text{ g}$, the first two units are in the 1 to 10 scale on the wirebonder.

The solution to the second problem simply involves inventing a way to insulate the barrier from the silicon to the puck. This was done by attaching a sapphire substrate to the Si-side of the sample. Sapphire was chosen because it is known to be a good insulator, and at the same time a good conductor of heat. Gold was deposited on the sapphire substrate to contact the silicon. In this deposition process, it must be made sure that no gold is on the sides of the sapphire plate, because conducting sidewalls of the plate can still provide a connection between the puck and the silicon, hence the sapphire plate would be rudimentary. This absence of gold on the sidewalls was ensured by putting extra silver paste on the sidewalls of the plate when attaching it to the sample holder of the Perkin Elmer sputtering system. The silicon (that was scratched in order to remove native oxides) on the back of the sample is connected with silver glue to the gold on the sapphire substrate. Now the back-gate contact can be connected to the gold, and no current can flow to the puck, which is connected to ground of the Physical Property Measurement System (PPMS). The puck with the sample and the backgate contact is shown in figure 3.5.

3.5 Measurement set-up

In order to do gate measurements on the sample at low temperatures, the sample is loaded into the PPMS (on a puck), which can cool down continuously to a temperature

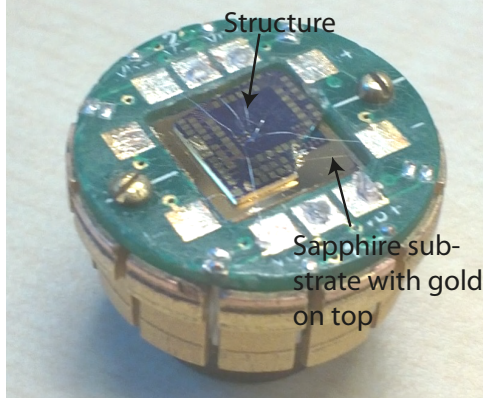


Figure 3.5: The measurement puck with the contacts to the gold on the sapphire and the contacts on the structure.

as low as 2 Kelvin and provide magnetic fields up to 9 Tesla. The currents were sourced externally, because the PPMS electronics are not designed to source current for small, delicate samples as were used in these experiments. Instead, lock-in amplifiers were used for the transport measurements by converting the voltage source into a current source with a resistance of $100\text{ k}\Omega$, which is much larger than the typical order of magnitude of the resistivity of the flakes ($1\text{ k}\Omega$). The voltage that was applied with the lock in amplifier was 0.1 V . With the resistance of $100\text{ k}\Omega$, this corresponds to sending a current of $I = 1\text{ }\mu\text{A}$.

Before choosing the suitable equipment for applying a gate voltage over the sample, one must calculate the potential needed to deplete all the carriers on the surface of the BSTS. This can be done by considering the parallel plate capacitor mentioned earlier on. We know that $Q = CU$, where Q is the amount of charge in Coulomb, C is the capacitance in Farad and U is the potential in Volts. Also, $C = \epsilon\epsilon_0 \frac{A}{d}$ and $Q = nAe$, here ϵ and ϵ_0 are the dielectric constant (of the SiO_2) and the electric constant respectively, A is the surface of the capacitor plate in m^2 , d is the distance between the two plates in m , n is the carrier density per unit surface in m^{-2} and e is the charge of an electron in Coulomb. n is known from previous experiments to be 10^{12} to 10^{13} cm^{-2} , the rest of the parameters are given. Combining these and solving for U gives the potential needed to completely deplete the TI surface of charge carriers: $U = \frac{ned}{\epsilon\epsilon_0} = 13.8$ to 138 V . This is a lot more than what the PPMS is wired for, which is around 25 V . Considering this upper limit, the system that is chosen to apply the gate voltage is a Keithley 2401, capable of sourcing voltages from -21 V to 21 V . A schematic of the set-up is shown in 3.6.

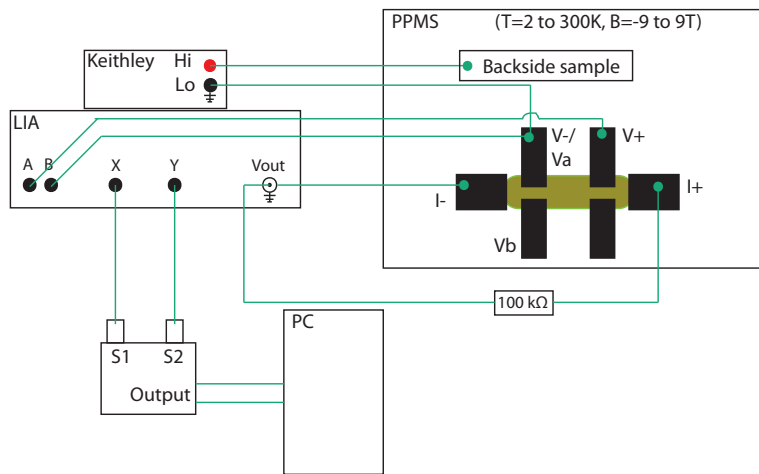


Figure 3.6: The set-up in a schematic representation. The input, A and B from the Lock in Amplifier (LIA) can also be connected to V_a and V_b for measurement of the Hall resistance

Chapter 4

Transport measurements on BSTS with an applied gate voltage

A back gate voltage was applied to BSTS in order to observe if the 2D carrier density at the surface of the BSTS, and by that, the Fermi level could be manipulated. Transport measurements have been done to obtain information about the position of the Fermi level, in order to observe whether it is placed in the gap or not.

It is important to note it is assumed that the surfaces of the topological insulator are effectively 2D, hence we use the following definition for the longitudinal resistivity: $\rho_{xx} = \frac{V_x}{I} \frac{W}{L}$, where in our case (because of the ill defined length and width of the flakes) $W \approx L$.

4.1 ρ_{xx} as a function of the temperature

For several flakes with varying thicknesses and shapes, the resistivity was measured as a function of temperature.

One can observe for flakes A and B (figure 4.2a and b) that upon lowering the temperature, the resistance first increases by a substantial amount, until around 100 K, when it suddenly starts decreasing again to a value of approximately 5 % of the maximum value below the maximum value. The increasing part can be interpreted as bulk temperature excitations freezing out (semiconductor behaviour) and one can fit this part with a function $\rho(T) = \rho_0 e^{\frac{\Delta}{k_B T}}$, from which one can extract Δ which represents the energy difference between the Fermi energy and the conduction band (figure 4.1). In this way, one can obtain information about the position of the Fermi level in the gap. When a certain temperature is reached, the surface contribution to the conductivity starts to prevail over the bulk contribution. The surface resistivity in this interpretation is assumed to be temperature independent. Note that the overall resistance of flake B is higher than that of flake A, this is probably due to the fact that flake B had the shape of a Hall bar, thus having smaller dimensions than flake A.

Flake C exhibits a different resistance as a function of temperature (figure 4.2c). One can observe that when cooling down from 300 K to 2 K, the change in resistance is relatively small (compared to Flake A and B). This small change in resistance over the whole temperature domain might indicate that we only observe a contribution from the surface, not from the bulk. This claim can be made stronger by observing that we cannot fit the inverse exponential dependence of the temperature, as can be done for semiconductors.

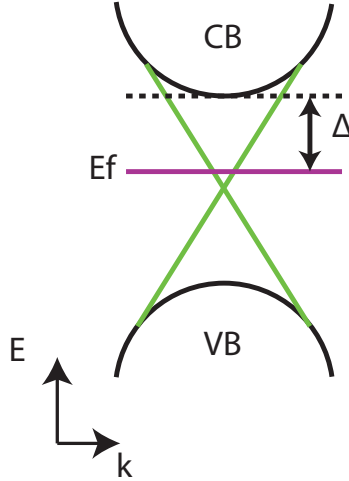


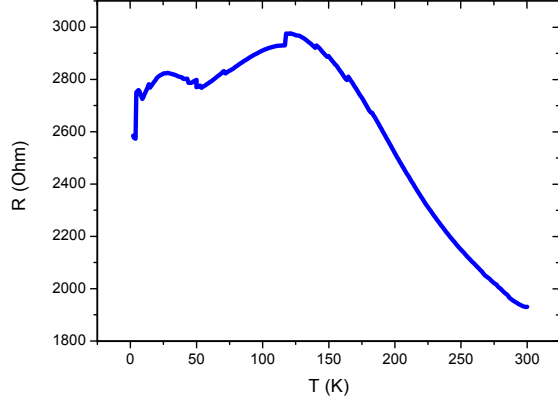
Figure 4.1: The energy Δ represents in this case the energy difference between the Fermi energy and the conduction band.

This eliminates the possibility of bulk conduction. The two peaks that are visible in the $R(T)$ plot can be a result of adsorption of impurities (such as water) on the surface of the BSTS. In the second $R(T)$ measurement, one week later, one can observe that the resistance at 300K has increased by more than 150 %. Also, the two peaks seem to almost have vanished.

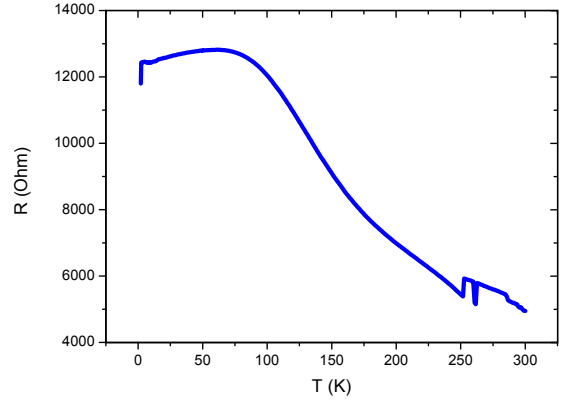
For flake D, a gate voltage of 21 Volts was applied during warm up and during cooldown a gate voltage was absent (figure 4.2). The result is striking; the dropping resistance from $T = 100$ K to 2 K that is claimed to be due to a prevailing surface contribution to conductivity is clearly split into two separate curves. The curve which belongs to the measurement where a gate voltage was applied shows a higher resistance; this could either be due the fact that charge carriers on the surface of the BSTS are depleted, or due to a difference in the mobility of the surface charge carriers. This will be investigated in the Hall measurement below. If we fit the inverse exponential temperature dependence of the resistivity and extract Δ , we find that $\Delta \approx 20$ meV.

All the $R(T)$ curves are different, which is surprising since all the measured flakes were mechanically exfoliated from the same BSTS crystal. Assuming that the band-structure of the material does not change, it seems as if the position of the Fermi level and the mobility differs per flake, as has been reported before [23]. It even changes over time, as seen for flake C, which was measured two times with a one week interval (stored in a transparent glass desiccator) between measurements. Possible explanations are H_2O adsorption on the surface, somehow influencing the conductivity, or photodoping.

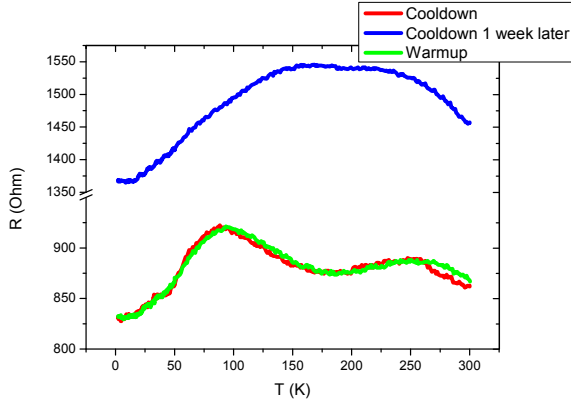
We can conclude that all the flakes might have a different height of the Fermi level, or have a different mobility but most of them show semiconducting behaviour at high temperature and surface conductivity at low temperatures, for flake D this claim is made stronger by a split curve at low temperatures.



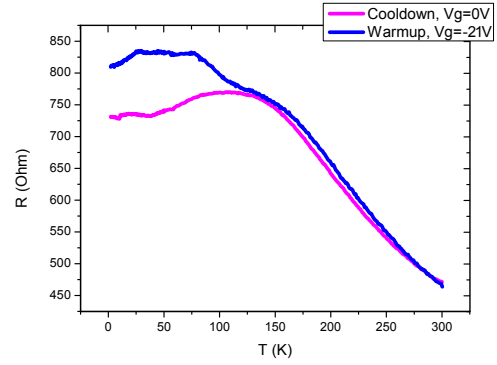
(a) Flake A, thickness of approximately 60 nm



(b) Flake B: A Hall bar shaped structure, note the high resistivity.



(c) Flake C, it seems to have no bulk contribution.



(d) Flake D, gated, a clear separation between surface and bulk contribution is seen.

Figure 4.2: Plots of the resistance as a function of temperature for different flakes.

4.2 ρ_{xx} as a function of the gate voltage

Resistance as a function of gate voltage has also been measured for flakes C and D, as shown in figure 4.3. Flakes A and B were destroyed before any gate measurements could be done.

For flake C one can observe that the gate voltage has less effect on the resistance at room temperature than it has at 2 Kelvin, this is expected, because the surface has a smaller contribution to the conductivity (compared to the bulk) at room temperature than it has at 2K. Note also the small discontinuity at $V_g = 0$ V. This discontinuity can be explained by considering that the gate voltage sweep was executed in two sequences: one from $V_g = 0$ to -21 V, and another from $V_g = 0$ to 21 V. In the first sweep, the material was ‘trained’ which resulted in a higher resistance at zero gate voltage; in other words, if the sweep was made from 0 to -21 to 0 to 21 to 0V, this loop would probably show hysteresis.

For flake D, the resistance as a function of the gate voltage is measured for three different temperatures. For temperatures 82 K and 300 K, the resistance was measured with a gate voltage with intervals of 5 V. For the 2 K measurement an interval of 1 V was used. One can observe that the slope of the curves is much steeper at 2 K than at 300 K, this difference is larger for flake D than for flake C. This is expected when observing the corresponding $R(T)$ curves, since flake C shows prevailing surface conductivity, even

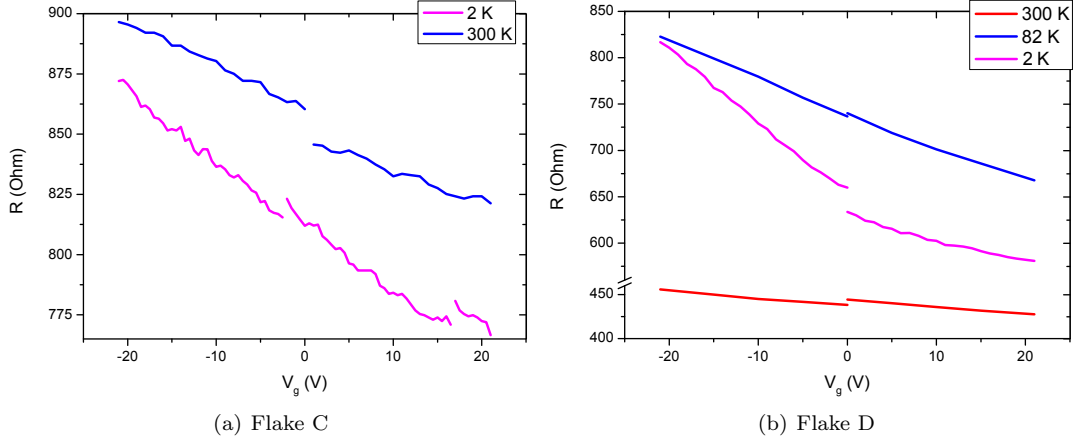


Figure 4.3: Resistance as a function of gate voltage. Note the discontinuities, caused by the trapped charge. It can be seen that for flake C, the flake with prevailing surface contribution, the angle between the curves for 2 K and 300 K is small as compared to the angle of the corresponding curves of flake D.

at 300 K, where flake D shows typical bulk behaviour at this temperature. Since the gate voltage only affects the surfaces, the difference between the 300 K and 2 K resistance as a function of gate voltage should be less for flake C than it is for flake D.

(The $\rho_{xx}(V_g)$ dependence at 2K for flake D shows some non-linear behaviour, this was also observed by Kim et al. [26] at low temperatures.)

4.3 Carrier density and mobility as a function of gate voltage

The Hall resistance of flake D was measured at 2 K as a function of magnetic field for three different values of the gate voltage, $V_g = -21, 0, 21$ V. From these field sweeps ($B = -2$ T to 2 T) the 2D carrier density and the mobility were determined via:

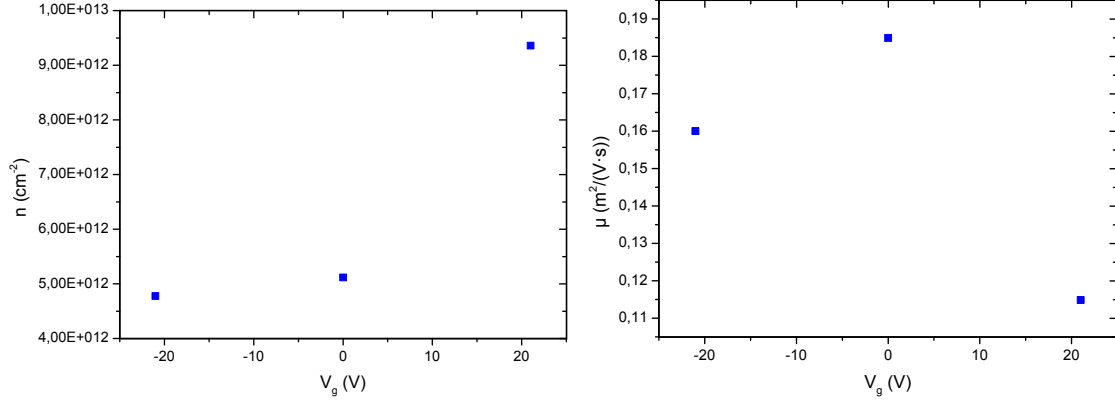
$$n_{2D} = \left[|e| \frac{d\rho_{xy}}{dB} \right]^{-1} \quad (4.1)$$

$$\mu = [|e| n_{2D} \rho_{xx}]^{-1} \quad (4.2)$$

Figure 4.4 shows the result of the Hall measurement. It can be seen that the carrier density decreases with an increasing gate voltage, as is expected because of the polarity of the applied gate voltage (depleting carriers in the surface with negative gate voltage). Quantitatively however, the charge carrier density increases only by 7 % from $V_g = -21$ V to 0 V, compared to the 81 % from 0 V to +21 V, which is not what is expected when one considers the substantial decrease in resistance from figure 4.3(b). This lack in change of carrier density seems to be compensated by the increase in mobility. It is still peculiar however that the mobility decreases by an amount of 37.8 % when the gate voltage is varied from 0 to +21 Volts. It is expected that with a varying gate voltage, the mobility will not be influenced and thus stay constant.

In trying to explain the varying mobility (from 0 to +21 Volts) as a function of gate voltage one could construct an argument like the following:

One can observe that the carrier density and the mobility are more or less constant for gate voltages of $V_g = -21$ V to 0 V. When the gate voltage is increased to 21 Volts, the carrier density increases by a substantial amount and the mobility drops to almost half of the initial value. This behaviour can be best understood when one considers the two surfaces (top and bottom) of the topological insulator separately.



(a) Carrier density. For $V_g = -21$ to 0 V , the carrier density difference is small in comparison to the difference between $V_g = -21$ to 0 V . (b) Mobility. The gate voltage seems for both polarities to have a negative effect on the mobility.

Figure 4.4: Carrier density and mobility for Flake D. Note that it is the trend that is important in these graphs, the numbers are not exact because of the ill-defined length and width of the flake.

For $V_g = -21$ and 0 V , we see that the value of the carrier density is approximately $n = 5 \times 10^{12} \text{ cm}^{-2}$, which is half of the value at $V_g = +21$ V . This could imply that for only one of the two surfaces the electrons are depleted for the lower two gate voltages. For $V_g = +21$ V , the electron density in the bottom surface is the same as the electron density in the top surface. This would imply that we only influence the bottom surface with the back gate. The drop in the mobility for $V_g = 21$ V can then be explained by assuming that the bottom surface of the BSTS has a smaller mobility than the top surface. If the amount of charge carriers is constant in the top surface and increases in the bottom surface, the transport is more and more mediated by the bottom surface, hence the total mobility of the BSTS flake is reduced.

This model is a little too crude however and leaves a few questions unanswered, like where the increase in resistance from $V_g = 0$ V to -21 V comes from, if the charge carrier density and the mobility of the charge carriers are being kept constant. Also: why, when all the electrons are depleted from the bottom surface (i.e. the Dirac point is reached), is the bottom surface not hole doped.

4.4 Conclusion and outlook

$R(T)$ curves of several flakes were measured and all of them showed different behaviour. One flake was measured two times with an interval of about a week, and even then showed a different $R(T)$ dependence. From this we can conclude that the BSTS is a material with a Fermi level that is easily shifted. A gate voltage was applied via the back of the sample and measurements showed that the longitudinal resistance over the sample is changed i.e. the gating has effect. Leakage currents were in the order of tens of pA 's which is the noise range in the voltage supply. It can be seen that the resistance increases with a decreasing voltage. Measurements of the charge carrier density show that the charge carriers are depleted with a decreasing gate voltage. The mobility of the BSTS is negatively influenced for both positive and negative gate voltage. This modulation in the charge carrier density shows that using a back gate possibly is a way to manipulate the height of the Fermi level. With this, experiments can also be done on a s-wave superconductor in proximity to a metal with SOC. One might be able to tune the Fermi level in the topologically non-trivial region and by that find Majorana fermions.

In the future it might be worth investigating what is the mechanism behind the change in mobility with a varying gate voltage. Also the mechanism behind the shifting resistance per flake and as a function of light/air exposure could be investigated, this might pave the way to more stable flakes of BSTS. In the future, when doing gate experiments, one should first sweep through the whole voltage domain, before doing any measurements as a function of gate voltage. This ensures the elimination of trapped charge and could prevent the discontinuities as encountered in figure 4.3.

For an exact measurement of the carrier density and mobility in BSTS as a function of gate voltage, well-defined Hall bars should be made using ebeam lithography. In future experiments one should make well-defined Hall bars using ebeam lithography. In order to completely eliminate the problem of the leakage current, one could consider the method of flip-chip electrical gating, as suggested by Kouwenhoven et al. In this configuration the gate structure is fabricated on a separate chip which is flipped and brought close (<100 nm) to the sample under research. A vacuum gap between the gates and material, acting as an insulating layer, solves the problem trapped charges as present in SiO_2 , and one can treat the sample much rougher than in the back-gating case.

Appendix A

Parameters for electron beam deposition

For an ebeam structure, an acceleration voltage of $20kV$ was used (the highest acceleration voltage available, while still being able to properly see the sample while applying the beam), the higher the voltage, the sharper the image. In figure A.1, the design of an ebeam structure can be seen. The smaller structures (light-green) were written with an aperture size of $10\ \mu m$ and a writing distance of $10\ mm$. The part of the smaller structures that are not on top of the BSTS flake received a dose of $220\ \mu C/cm^2$. The part of the contacts that lay on top of the BSTS received a dose of 180 to $200\ \mu C/cm^2$. The difference between the two doses originates from the fact that the BSTS reflects electrons more strongly than the SiO_2 , which results in a higher reflected dose for the PPMA, so a lower overall dose is needed.

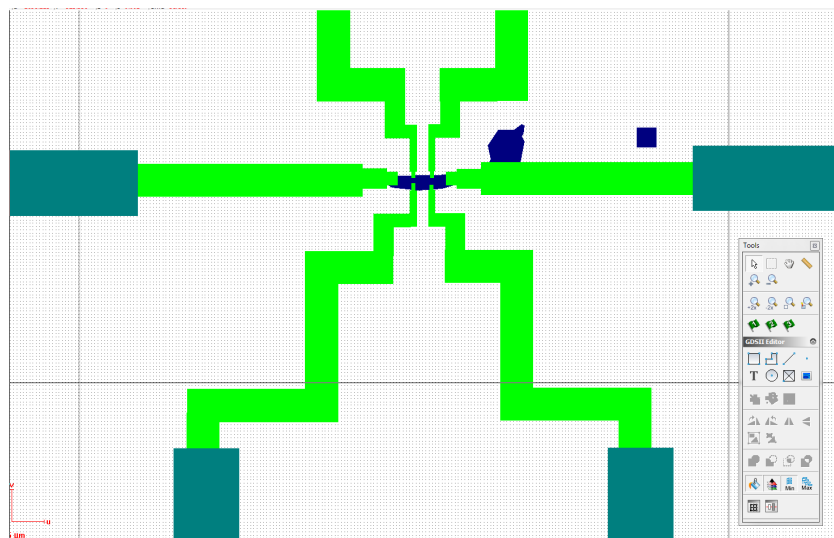


Figure A.1: A design made in the RAITH-software, for the contacts to the flake.

Acknowledgements

I learned so much from the time in this group. I am very thankful to a lot of people, probably more than I can write down here. I would like to thank Marieke Snelder for being a great advisor. I really enjoyed the discussions and the fact that I could run into your office at any given moment and have my question answered by you directly, I also appreciate the patience with which you have introduced me into the NanoLab. The best of luck on the gating experiment, and combining it with a superconductor. I would like to thank Alexander for being an incredibly motivating professor. I often left your office again in an excited state. I liked discussing with you, and how you can find the interesting elements in my results, experimental or theoretical. I found that very motivating. Thank you Geert Brocks for being willing to be my external commission member.

I would like to thank Martin, for helping out with the problem of the leakage current, you were very valuable to this project. I would like to thank Cor for answering a lot of questions even if you were busy typing your thesis in deep concentration, and for being a very pleasant roommate. Thank you Dick and Frank for all the patience in helping out in the lab. Thank you Julius, for carefully reading the manuscript in your spare time and for the discussions on high brow and low brow subjects. Thanks Ankur for the great dinners and the discussions about theory and subjects that go beyond that. Thanks Roel and Thijs for being delightful roommates. Thanks everybody from ICE that I did not mention here, I enjoyed the atmosphere a lot, and the sailing trip was great.

I would like to thank Maurice and Mike for the exchange of good ideas, the music, the gardening, the walks in the woods. I liked hanging out with you from the beginning of our studies. I thank all my friends from technische natuurkunde. Thanks to my friends from the Box, Tim, Michel, Allard, Jonah, Emiel, Jay, Peter. Living in a box is a pleasure with you. Thanks to my friends from Amsterdam, soon we will surf the waves again. Thanks to Zengroep Hengelo and Piranha.

I want to thank my family, especially my parents who constantly supported me so lovingly in everything I wanted to pursue. Thank you.

Enschede, February 2014

Bibliography

- [1] E. Majorana. Teoria simmetrica dellelettrone e del positrone. *Nuovo Cimento*, (14):171, 1937.
- [2] Frank Wilczek. Majorana returns. *Nature Physics*, 5(9):614–618, September 2009.
- [3] W Keung and G Senjanovic. Majorana Neutrinos and the Production of the Right-Handed Charged Gauge Boson. *Phys. Rev. Lett.*, 50(19):1427–1430, 1983.
- [4] Liang Fu and CL Kane. Superconducting proximity effect and Majorana fermions at the surface of a topological insulator. *Physical review letters*, (3):1–4, 2008.
- [5] H.K. Onnes. The resistance of pure mercury at helium temperatures. *Commun. Phys. Lab. Univ. Leiden*, 12:120, December 1911.
- [6] LN Cooper. Bound electron pairs in a degenerate Fermi gas. *Physical Review*, 104(4):1–2, 1956.
- [7] Jason Alicea. New directions in the pursuit of Majorana fermions in solid state systems. *Reports on progress in physics. Physical Society (Great Britain)*, 75(7):076501, July 2012.
- [8] Martin Leijnse and Karsten Flensberg. Introduction to topological superconductivity and Majorana fermions. *Semiconductor Science and Technology*, 27(12):124003, December 2012.
- [9] K. v. Klitzing, G. Dorda, and M. Pepper. New method for high-accuracy determination of the fine-structure constant based on quantized Hall resistance. *Physical Review Letters*, 1980.
- [10] Shuichi Murakami, Naoto Nagaosa, and Shou-Cheng Zhang. Dissipationless quantum spin current at room temperature. *Science (New York, N.Y.)*, 301(5638):1348–51, September 2003.
- [11] M.I. D'yakonov and V.I. Perel. No. *JETP Lett.*, 13:467, 1971.
- [12] Y K Kato, R C Myers, a C Gossard, and D D Awschalom. Observation of the spin Hall effect in semiconductors. *Science (New York, N.Y.)*, 306(5703):1910–3, December 2004.
- [13] M.V. Berry. Quantal Phase Factors Accompanying Adiabatic Changes. *Proceedings of the Royal Society*, 392(1802):45–57, 1984.
- [14] XL Qi and SC Zhang. The quantum spin Hall effect and topological insulators. *Physics Today*, (January):33–38, 2010.
- [15] B Andrei Bernevig, Taylor L Hughes, and Shou-Cheng Zhang. Quantum spin Hall effect and topological phase transition in HgTe quantum wells. *Science (New York, N.Y.)*, 314(5806):1757–61, December 2006.

- [16] Markus König, Steffen Wiedmann, Christoph Brüne, Andreas Roth, Hartmut Buhmann, Laurens W Molenkamp, Xiao-Liang Qi, and Shou-Cheng Zhang. Quantum spin hall insulator state in HgTe quantum wells. *Science (New York, N.Y.)*, 318(5851):766–70, November 2007.
- [17] Liang Fu and C. Kane. Topological insulators with inversion symmetry. *Physical Review B*, 76(4):045302, July 2007.
- [18] Yoichi Ando. Topological Insulator Materials. *arXiv preprint arXiv:1304.5693*, 2013.
- [19] D Hsieh, D Qian, L Wray, Y Xia, Y S Hor, R J Cava, and M Z Hasan. A topological Dirac insulator in a quantum spin Hall phase. *Nature*, 452(7190):970–4, April 2008.
- [20] a. Taskin and Yoichi Ando. Quantum oscillations in a topological insulator Bi_{1-x}Sb_x. *Physical Review B*, 80(8):085303, August 2009.
- [21] Haijun Zhang, Chao-Xing Liu, Xiao-Liang Qi, Xi Dai, Zhong Fang, and Shou-Cheng Zhang. Topological insulators in Bi₂Se₃, Bi₂Te₃ and Sb₂Te₃ with a single Dirac cone on the surface. *Nature Physics*, 5(6):438–442, May 2009.
- [22] M. Z. Hasan and C. L. Kane. Colloquium: Topological insulators. *Reviews of Modern Physics*, 82(4):3045–3067, November 2010.
- [23] a. a. Taskin, Zhi Ren, Satoshi Sasaki, Kouji Segawa, and Yoichi Ando. Observation of Dirac Holes and Electrons in a Topological Insulator. *Physical Review Letters*, 107(1):016801, June 2011.
- [24] T Arakane, T Sato, S Souma, K Kosaka, K Nakayama, M Komatsu, T Takahashi, Zhi Ren, Kouji Segawa, and Yoichi Ando. Tunable Dirac cone in the topological insulator Bi(2-x)Sb(x)Te(3-y)Se(y). *Nature communications*, 3:636, January 2012.
- [25] Liang Fu. Hexagonal Warping Effects in the Surface States of the Topological Insulator Bi₂Te₃. *Physical Review Letters*, 103(26):266801, December 2009.
- [26] Dohun Kim, Sungjae Cho, Nicholas P. Butch, Paul Syers, Kevin Kirshenbaum, Shafiqe Adam, Johnpierre Paglione, and Michael S. Fuhrer. Surface conduction of topological Dirac electrons in bulk insulating Bi₂Se₃. *Nature Physics*, 8(6):460–464, April 2012.
- [27] Kouji Segawa, Zhi Ren, Satoshi Sasaki, Tetsuya Tsuda, Susumu Kuwabata, and Yoichi Ando. Ambipolar transport in bulk crystals of a topological insulator by gating with ionic liquid. *Physical Review B*, 86(7):075306, August 2012.
- [28] V Mourik, K Zuo, S M Frolov, S R Plissard, E P a M Bakkers, and L P Kouwenhoven. Signatures of Majorana fermions in hybrid superconductor-semiconductor nanowire devices. *Science (New York, N.Y.)*, 336(6084):1003–7, May 2012.
- [29] Jay D. Sau, Roman M. Lutchyn, Sumanta Tewari, and S. Das Sarma. Generic New Platform for Topological Quantum Computation Using Semiconductor Heterostructures. *Physical Review Letters*, 104(4):040502, January 2010.
- [30] Roman M. Lutchyn, Jay D. Sau, and S. Das Sarma. Majorana Fermions and a Topological Phase Transition in Semiconductor-Superconductor Heterostructures. *Physical Review Letters*, 105(7):077001, August 2010.
- [31] Yuval Oreg, Gil Refael, and Felix von Oppen. Helical Liquids and Majorana Bound States in Quantum Wires. *Physical Review Letters*, 105(17):177002, October 2010.

- [32] Jason Alicea. Majorana fermions in a tunable semiconductor device. *Physical Review B*, 81(12):125318, March 2010.
- [33] Jie Liu, AC Potter, KT Law, and PA Lee. Zero-bias peaks in spin-orbit coupled superconducting wires with and without Majorana end-states. *arXiv preprint arXiv:1206.1276*, pages 18–20, 2012.
- [34] Leonid P. Rokhinson, Xinyu Liu, and Jacek K. Furdyna. The fractional a.c. Josephson effect in a semiconductor-superconductor nanowire as a signature of Majorana particles. *Nature Physics*, 8(11):795–799, September 2012.
- [35] J Bardeen, L.N. Cooper, and J.R. Schrieffer. Microscopic Theory of Superconductivity. *Phys. Rev.*, (106):162–164, 1957.
- [36] J Bardeen, L.N. Cooper, and J.R. Schrieffer. Theory of superconductivity. *Physical Review*, (108):1175–1204, 1957.
- [37] Alexander Altland and Ben Simons. *Condensed Matter Field Theory*. 2010.
- [38] Geert Brocks. *Advanced Quantum Mechanics*. 2002.
- [39] Nikolai Bogolyubov. On the theory of superfluidity. *J. Phys. (USSR)*, (11):23, 1947.
- [40] Miguel Ibañez, John Links, Germán Sierra, and Shao-You Zhao. Exactly solvable pairing model for superconductors with a p+ip-wave symmetry. B79(180501), 2009.
- [41] a.P Mackenzie and Y Maeno. P-Wave Superconductivity. *Physica B: Condensed Matter*, 280(1-4):148–153, May 2000.
- [42] Wolfgang Pauli. Zur Quantenmechanik des magnetischen Elektrons. *Zeitschrift für Physik*, (43):601–623, 1927.
- [43] E.I. Rashba. Properties of semiconductors with an extremum loop. *Sov. Phys. Solid state*, 1960.
- [44] R. Holm and W. Meissner. No Title. *Z. Physik*, (74):715, 1932.
- [45] L Petersen and P Hedegård. A simple tight-binding model of spin-orbit splitting of sp-derived surface states. *Surface science*, 459:49–56, 2000.
- [46] S LaShell, Ba McDougall, and E Jensen. Spin Splitting of an Au(111) Surface State Band Observed with Angle Resolved Photoelectron Spectroscopy. *Physical review letters*, 77(16):3419–3422, October 1996.
- [47] Andrew C. Potter and Patrick a. Lee. Engineering a p+ip superconductor: Comparison of topological insulator and Rashba spin-orbit-coupled materials. *Physical Review B*, 83(18):184520, May 2011.
- [48] Matthias Eschrig, Christian Iniotakis, and Yukio Tanaka. Theoretical aspects of Andreev spectroscopy and tunneling spectroscopy in non-centrosymmetric superconductors: a topical review. *arXiv preprint arXiv:1001.2486*, 2010.
- [49] Andrew C. Potter and Patrick a. Lee. Topological superconductivity and Majorana fermions in metallic surface states. *Physical Review B*, 85(9):094516, March 2012.
- [50] K S Novoselov, a K Geim, S V Morozov, D Jiang, M I Katsnelson, I V Grigorieva, S V Dubonos, and a a Firsov. Two-dimensional gas of massless Dirac fermions in graphene. *Nature*, 438(7065):197–200, November 2005.